

UC Irvine

UC Irvine Previously Published Works

Title

Condensed-phase biogenic–anthropogenic interactions with implications for cold cloud formation

Permalink

<https://escholarship.org/uc/item/0xq9x6w7>

Authors

Charnawskas, Joseph C

Alpert, Peter A

Lambe, Andrew T

et al.

Publication Date

2017-08-24

DOI

10.1039/c7fd00010c

Copyright Information

This work is made available under the terms of a Creative Commons Attribution License, available at

<https://creativecommons.org/licenses/by/4.0/>

Peer reviewed

Condensed-phase biogenic–anthropogenic interactions with implications for cold cloud formation

Joseph C. Charnawskas,^a Peter A. Alpert,^{†a} Andrew T. Lambe,^{bc} Thomas Berkemeier,^d Rachel E. O'Brien,^{‡ef} Paola Massoli,^c Timothy B. Onasch,^{id bc} Manabu Shiraiwa,^g Ryan C. Moffet,^f Mary K. Gilles,^e Paul Davidovits,^b Douglas R. Worsnop^c and Daniel A. Knopf^{id *a}

Received 11th January 2017, Accepted 24th January 2017

DOI: 10.1039/c7fd00010c

Anthropogenic and biogenic gas emissions contribute to the formation of secondary organic aerosol (SOA). When present, soot particles from fossil fuel combustion can acquire a coating of SOA. We investigate SOA–soot biogenic–anthropogenic interactions and their impact on ice nucleation in relation to the particles' organic phase state. SOA particles were generated from the OH oxidation of naphthalene, α -pinene, longifolene, or isoprene, with or without the presence of sulfate or soot particles. Corresponding particle glass transition (T_g) and full deliquescence relative humidity (FDRH) were estimated using a numerical diffusion model. Longifolene SOA particles are solid-like and all biogenic SOA sulfate mixtures exhibit a core–shell configuration (i.e. a sulfate-rich core coated with SOA). Biogenic SOA with or without sulfate formed ice at conditions expected for homogeneous ice nucleation, in agreement with respective T_g and FDRH. α -pinene SOA coated soot particles nucleated ice above the homogeneous freezing temperature with soot acting as ice nuclei (IN). At lower temperatures the α -pinene SOA coating can be semisolid, inducing ice nucleation. Naphthalene SOA coated soot particles acted as ice nuclei above and below the homogeneous freezing limit, which can be explained by the presence of a highly viscous SOA phase. Our results suggest that biogenic SOA does not play a significant

^aInstitute for Terrestrial and Planetary Atmospheres, School of Marine and Atmospheric Sciences, Stony Brook University, Stony Brook, New York, USA. E-mail: Daniel.Knopf@stonybrook.edu

^bChemistry Department, Boston College, Chestnut Hill, Massachusetts, USA

^cAerodyne Research Inc., Billerica, Massachusetts, USA

^dSchool of Chemical and Biomolecular Engineering, Georgia Institute of Technology, Atlanta, Georgia, USA

^eChemical Sciences Division, Lawrence Berkeley National Laboratory, Berkeley, USA

^fDepartment of Chemistry, University of the Pacific, Stockton, California, USA

^gDepartment of Chemistry, University of California, Irvine, California, USA

[†] Present address: Laboratory of Environmental Chemistry, Paul Scherrer Institute, Villigen, Switzerland.

[‡] Present address: Department of Civil and Environmental Engineering, Massachusetts Institute of Technology, Cambridge, USA.

role in mixed-phase cloud formation and the presence of sulfate renders this even less likely. However, anthropogenic SOA may have an enhancing effect on cloud glaciation under mixed-phase and cirrus cloud conditions compared to biogenic SOA that dominate during pre-industrial times or in pristine areas.

1 Introduction

Aerosol particles play an important role in the radiative budget of the Earth by scattering and absorbing short wave and long wave radiation and modifying the radiative properties of clouds by acting as cloud condensation (CCN) nuclei and IN.^{1–3} Furthermore, glaciation of clouds plays a crucial role in precipitation and thus the hydrological cycle.⁴ However, the magnitude of aerosol climate forcing remains highly uncertain. These uncertainties are attributed to the different scales involved in microphysical processes as well as in the various ice crystal formation pathways in cold clouds.^{2,5} The impact of biogenic and anthropogenic particulate matter (separately and together) on atmospheric ice nucleation remains insufficiently understood. This knowledge is crucial not only to improve predictive understanding of our current climate, but also to better establish cold cloud formation during pre-industrial times⁶ where sulfate and anthropogenic emissions were much lower.⁷

SOA is formed by the condensation of semi-volatile and low volatility products of oxidized volatile organic compounds (VOCs) stemming from anthropogenic and biogenic sources.^{8–13} Although the majority of VOCs are biogenic,^{14–16} increasing population and urbanization¹⁷ will likely increase anthropogenic VOC emissions.¹⁸ Recently it has been recognized that organic particles can exist in amorphous solid (glassy), semisolid, or liquid phase states depending upon their T_g ^{19–24} and relative humidity (RH).^{25–28} In addition, the OA particle phase state affects the particles' ability to act as IN.^{19,29–31} Soot particles formed from the incomplete combustion of fossil fuels and biomass burning are abundant in the atmosphere with a large fraction being anthropogenic.³² Soot particles can also change the properties and lifecycle of mixed-phase and ice clouds.^{32–35}

Ice crystals can form *via* homogeneous or heterogeneous nucleation. Homogeneous ice nucleation occurs from a supercooled aqueous droplet at temperatures below ~ 238 K.³⁶ Compared to homogeneous ice nucleation, the presence of IN induces heterogeneous ice nucleation at higher temperatures and lower RH with respect to ice (RH_{ice}).³⁶ Heterogeneous ice nucleation can occur *via* immersion freezing (ice nucleates on IN immersed in a supercooled aqueous droplet) and deposition ice nucleation on a particle (ice nucleates from the supersaturated gas phase onto IN). Under mixed-phase cloud conditions, immersion freezing is thought to be the dominant freezing mechanism,³⁷ whereas cirrus clouds can form *via* homogeneous and deposition ice nucleation and immersion freezing.^{38–40}

Previous studies have demonstrated that ice crystal residues in cirrus and mixed-phase clouds can contain organic materials.^{39,41–47} Laboratory ice nucleation experiments have demonstrated the ability of different types of OA and SOA particles to nucleate ice.^{23,29,31,48–57} Wang *et al.* (2012)³¹ demonstrated that SOA produced from gas-phase OH oxidation of naphthalene, an anthropogenic aromatic VOC, act as deposition IN at temperatures below 230 K and as

immersion IN at temperatures between 230 and 245 K. SOA particles produced from the ozonolysis of α -pinene are considered inefficient IN.^{51,52} However, other studies that pre-cooled the particles to ensure a solid phase^{50,51} found that α -pinene derived SOA can act as IN. Lienhard *et al.* (2015)²⁹ suggested that α -pinene SOA particles only act as IN for lowest atmospheric temperatures and fast updrafts. However, in that study the SOA particles were derived from OH oxidation rather than exposure to O₃. Prenni *et al.* (2009)⁴⁶ showed that SOA produced from the ozonolysis of alkenes did not yield detectable quantities of IN at 243 K.

Several laboratory studies have investigated soot particles acting as IN as a function of soot type, origin, and experimental ice nucleation conditions.^{58–75} Generally, soot particles are not as efficient IN compared to, *e.g.*, mineral dust particles. Three studies have examined the role of mono-/dicarboxylic acid and SOA coatings on the ice nucleation propensity of soot particles. Friedman *et al.* (2011)⁶⁷ investigated both uncoated soot particles and those coated with adipic, malic, and oleic acids, exposed to atmospherically relevant amounts of O₃, and found no evidence of heterogeneous ice nucleation between 253 and 243 K and only homogeneous freezing at 233 K. Kulkarni *et al.* (2016)⁷³ observed that soot particles coated with SOA derived from α -pinene + OH nucleated ice at homogeneous freezing conditions. Chou *et al.* (2013)⁵⁹ observed soot particles coated with SOA produced from mixed α -pinene and diesel exhaust emissions to nucleate ice at 238 K and above water saturation. These recent studies suggest that soot coated by SOA material does not impact heterogeneous ice nucleation significantly.

In this study, by examining the thermodynamic conditions under which ice forms, we investigate SOA–soot biogenic–anthropogenic interactions and their impacts on ice nucleation. Biogenic SOA is generated from the OH oxidation of α -pinene, longifolene, or isoprene, with or without the presence of SO₄. Anthropogenic SOA is generated from the OH oxidation of naphthalene. Additionally, laboratory generated soot particles are coated by α -pinene or naphthalene SOA. SOA coating thicknesses and SOA oxidation levels are varied. Scanning electron microscopy (SEM) is applied to obtain images of the deposited particles. The particle mixing state is evaluated by scanning transmission X-ray microscopy with near edge X-ray absorption spectroscopy (STXM/NEXAFS).^{76–78} To probe the particles' propensity to act as IN, ice nucleation is investigated as a function of temperature as low as 210 K and RH_{ice} as high as water saturation.⁷⁹ In addition, a numerical diffusion model^{19,80} is applied to estimate T_g and the FDRH of the SOA particles as a function of SOA type, amount of sulfate, soot core size, SOA coating thickness, level of oxidation, and updraft velocities for typical atmospheric conditions. The simulated SOA phase state properties allow us to assess our predictive understanding of the impact of amorphous biogenic SOA and anthropogenic SOA as well as SOA coated sulfate and soot particles on atmospheric ice formation.

2 Methods

2.1 Particle production and sampling

Soot particles were generated using an inverted diffusion burner flame as described in detail elsewhere.^{81–85} Flows of methane and air were delivered to the burner at flow rates of 1.26 and 17.6 L min⁻¹, respectively, with a global

equivalence ratio of 0.7. Following dilution into 30 L min^{-1} nitrogen, a mini-educator (Fox Valves) extracted a flow of polydisperse soot particles from the flame tip. Gas-phase organics were removed by passing the flow through a charcoal denuder. OH radicals were produced in a Potential Aerosol Mass (PAM) oxidation flow reactor^{86,87} from the reaction $\text{O}_3 + h\nu \rightarrow \text{O}_2 + \text{O}^1(\text{D})$ ($\lambda = 254 \text{ nm}$) followed by the reaction $\text{O}^1(\text{D}) + \text{H}_2\text{O} \rightarrow 2 \text{ OH}$. Inside the PAM reactor, four low-pressure mercury lamps generated UV light; the temperature inside the reactor ranged from 22 to 30 °C as a function of UV intensity. Outside of the PAM reactor, O_2 was irradiated with a mercury lamp ($\lambda = 185 \text{ nm}$) to produce O_3 . A Nafion® membrane humidifier with a controlled RH of 24–30% was used to humidify the nitrogen carrier gas. The biogenic and anthropogenic precursor gases α -pinene, longifolene, isoprene, naphthalene, and/or SO_2 were introduced to generate oxidized vapours *via* OH oxidation inside the PAM reactor that either homogeneously nucleated to form SOA/sulfate particles or formed a deposition coating on soot particles (if present). The coating thickness was modified by varying the VOC precursor concentration and monitored by subsequent particle size examination. Mass spectra and vacuum aerodynamic size distributions of the SOA coated soot particles were obtained using an Aerodyne soot particle time-of-flight aerosol mass spectrometer (SP-AMS) operated in V-mode.⁸⁸ The mass spectra were analysed using ToF-AMS analysis software (SQUIRREL and PIKA⁸⁹) which yielded high-resolution mass spectra and organic, sulfate, and refractive black carbon loadings. The oxygen-to-carbon ratio (O/C), used here as a measurable surrogate of the particle oxidation level, was calculated using methods described by Canagaratna *et al.* (2015).⁹⁰ The mobility size distribution was obtained using a Scanning Mobility Particle Sizer (SMPS).

2.2 Particle collection

Particles were collected onto substrates using a multi-orifice uniform deposition impactor (MOUDI, model 122R) equipped with 13 rotating impaction stages.^{78,79,91} The substrates for the collection of particles were placed on stage 7 (50% cut-point of 320 nm) and on stage 8 (50% cut-point of 180 nm) for biogenic SOA.⁹² Simultaneously, particles were collected on silicon (Si) wafer chips (Silson, Inc.), 50 nm carbon films supported on copper grids (“Carbon Type-B” grid substrates, Ted Pella, Inc.), silicon nitride coated frames (“ Si_3N_4 -film” substrates, Silson, Inc.), and hydrophobically coated glass slides.^{31,93} Particles were stored in aluminium containers placed inside airtight plastic bags filled with N_2 . Samples were transported and stored at 3 °C until use. Ice nucleation experiments were performed using the hydrophobically coated glass slides and Si wafer chips; SEM and STXM were performed on the Si_3N_4 -film substrates and copper grids.

Biogenic SOA particle mean particle diameter (D), particle number density present on the substrate (N), and total particle surface area (A_{ice}) involved in the ice nucleation experiment were estimated from SEM images (Table 1). For the SOA coated soot particles, D , N , and A_{ice} (Table 2) were determined using optical microscopy.⁹³ By treating the particles as hemispheres, the diameters were determined from the 2-dimensional particle projected area (A), $D = 2(A/\pi)^{1/2}$. Total particle surface area (SA) was derived from D , particle number density, and $A_{\text{ice}} = 0.79 \text{ mm}^2$, $\text{SA} = 1/2\pi D^2 N A_{\text{ice}}$.

Table 1 Sample characteristics of biogenic SOA particles used in SEM images, ice nucleation experiments, and corresponding model simulations. The oxygen-to-carbon (O/C) ratio is a measurable surrogate of the SOA oxidation level. $T_{g,org}$ is the glass transition temperature of the SOA under dry conditions. κ represents the hygroscopicity parameter, ρ is density, D is the mean particle diameter, N represents the particle number density present on the substrate, and SA is the total particle surface area

Precursor	O/C ^a	Organic-to-sulfate ratio	Model layers	$T_{g,org}^c$ (K)	$\kappa^{d,e}$	ρ^e (g cm ⁻³)	D^f (μ m)	N^f ($\times 10^6$ mm ⁻²)	SA^f ($\times 10^{-2}$ mm ²)
α -Pinene	0.74 \pm 0.21		300	334.3	0.16 \pm 0.03	1.44 \pm 0.29	0.17 \pm 0.09	2.77 \pm 0.68	13.1 \pm 19.3
α -Pinene + SO ₂	0.69 \pm 0.20	5 : 1	300	311.7	0.21 \pm 0.04	1.46 \pm 0.29	0.17 \pm 0.06	4.12 \pm 1.05	17.1 \pm 9.6
Longifolene	0.45 \pm 0.13						0.16 \pm 0.01	2.63 \pm 0.68	10.9 \pm 1.6
Longifolene + SO ₂	0.46 \pm 0.13	5.6 : 1					0.21 \pm 0.04	2.32 \pm 0.60	12.5 \pm 5.1
Isoprene	0.81 \pm 0.23 ^b						0.17 \pm 0.07	3.14 \pm 0.78	13.1 \pm 12.1
Isoprene + SO ₂	0.54 \pm 0.15 ^b	8 : 1					0.23 \pm 0.05	2.62 \pm 0.68	17.8 \pm 9.3

^a Uncertainty in O/C ratio was estimated to be 28%,³⁰ ^b Chen *et al.* (2011),¹²⁹ ^c Zobrist *et al.* (2008),¹²⁸ Berkemeier *et al.* (2014),¹⁹ ^d Lambe *et al.* (2011),¹¹⁰ ^e Uncertainty in ρ ¹³⁰ and κ ¹³¹ were estimated to be ~20%,^f Uncertainty represents one standard deviation (1σ).

Table 2 Sample characteristics of biogenic and anthropogenic SOA coated soot particles used in ice nucleation experiments and corresponding model simulations. The oxygen-to-carbon (O/C) ratio is a measurable surrogate of the SOA oxidation level. $T_{g,org}$ is the glass transition temperature of the SOA under dry conditions. κ represents the hygroscopicity parameter. ρ is density, D is the mean particle diameter, N represents the particle number density present on the substrate, and SA is the total particle surface area

Precursor	O/C ^a	Soot core (nm)	Coating thickness (nm)	Model layers	$T_{g,org}^b$ (K)	$\kappa_{org}^{c,d}$	$\rho^{d,e}$ (g cm ⁻³)	$D^{f,g}$ (μ m)	N^g ($\times 10^4$ mm ⁻²)	SA ^g ($\times 10^{-2}$ mm ²)
α -Pinene	0.45 \pm 0.13	110	9	30	266.1 \pm 6.9	0.11 \pm 0.02	1.2 \pm 0.2	0.92 \pm 0.14	4.75 \pm 1.38	4.98 \pm 1.62
α -Pinene	0.42 \pm 0.12	229	68	226	258.6 \pm 7.2	0.11 \pm 0.02	1.14 \pm 0.22	0.86 \pm 0.11	8.78 \pm 2.30	8.09 \pm 2.35
α -Pinene	0.64 \pm 0.18	188	30	100	313.2 \pm 10.5	0.15 \pm 0.03	1.27 \pm 0.25	0.85 \pm 0.10	3.76 \pm 0.66	3.39 \pm 0.72
α -Pinene	0.59 \pm 0.17	128	66	220	300.8 \pm 8.8	0.14 \pm 0.03	1.24 \pm 0.25	0.82 \pm 0.10	8.50 \pm 1.72	7.15 \pm 1.70
Naphthalene	0.44 \pm 0.12	178	53	176	307.5 \pm 7.2	0.11 \pm 0.02	1.34 \pm 0.27	0.78 \pm 0.11	4.30 \pm 1.39	3.26 \pm 1.15
Naphthalene	0.40 \pm 0.11	223	76	253	303.7 \pm 6.5	0.10 \pm 0.02	1.34 \pm 0.27	0.77 \pm 0.11	12.14 \pm 3.09	9.04 \pm 2.65
Naphthalene	1.03 \pm 0.29	135	76	253	363.2 \pm 24.4	0.22 \pm 0.05	1.57 \pm 0.31	0.81 \pm 0.09	12.30 \pm 3.14	9.96 \pm 2.75

^a Uncertainty in O/C ratio was estimated to be 28%.⁹⁰ ^b Berkemeier *et al.* (2014).¹⁹ ^c Lambe *et al.* (2011).¹¹⁰ ^d Uncertainty in ρ^{130} and κ^{131} were estimated to be \sim 20%.
^e Kuwata *et al.* (2011).¹³² ^f Uncertainty represents one standard deviation (1 σ) and does not include instrumental uncertainty of at least 0.2 μ m. ^g Particles smaller than 0.4 μ m cannot be detected using optical microscopy and the particle density should be considered as a lower limit. Uncertainty represents one standard deviation (1 σ).

2.3 Particle characterization by STXM/NEXAFS analysis

STXM/NEXAFS was used to determine the particle composition and mixing state, similar to our previous studies.^{76–79,94,95} The chemical composition and mixing state of individual particles is determined from spatially resolved X-ray spectra.^{76,96–100} The spatial resolution was about 30–40 nm. The identification of organic carbon, elemental carbon (soot), and inorganic components is possible by examining the carbon K-edge spectra, which allows for the classification of particle types as well as their mixing states.⁹⁵ Technical details of STXM, as well as the application of STXM on atmospheric particles, are published elsewhere.^{77,101–103}

2.4 Ice nucleation apparatus

Ice nucleation experiments were performed using a custom-built controlled vapour cryo-cooling stage microscope system described in detail elsewhere.^{79,93,94} Visual identification of ice formation was determined by changes in particle phase or size greater than 0.2 μm (1130 \times magnification) and 1 μm (230 \times magnification). A digital camera recorded particle images every 0.02 K. Initial ice formation events are reported and the experimental time, particle temperature (T_p), and dew point (T_d) were recorded. T_d was set by flowing 1 SLPM (standard litre per minute) humidified N_2 gas (ultrahigh purity and passing through a cryo-trap) over the particles. $\text{N}_2(\text{g})$ exited the ice nucleation cell and T_d was measured using a chilled mirror hygrometer (GE Sensing 1311DR). RH_{ice} was calculated from the measured T_p and T_d values.¹⁰⁴ After detection of ice crystals, T_p was calibrated following established methods^{65,93,105,106} by observing the growth and sublimation of the ice crystals by variation of T_p . Experimental uncertainties of $\Delta T_d < \pm 0.15$ K and $\Delta T_p < \pm 0.3$ K yield conservative (the maximum difference between T_p and T_d) RH_{ice} uncertainties of less than $\pm 11\%$ at 200 K and $\pm 3\%$ at 260 K.^{93,94} The reported ice nucleation data represent the measurement of 1–6 independent experiments per temperature range investigated.

2.5 Experimental procedure

An ice nucleation experiment started at subsaturated conditions with respect to ice, with RH_{ice} typically between 85 and 90%. Then, T_p was decreased at a rate of 0.1 or 0.2 K min^{-1} . This rate corresponds to cooling rates associated with updraft velocities characteristic of mid-latitude and low-latitude cirrus clouds.^{107–109} These slower changes in RH_{ice} allow for the assessment of the importance of amorphous solid and semisolid organic materials to act as IN. This is relevant because at faster updraft velocities (*i.e.* a faster change in RH_{ice}), the threshold RH_{ice} for nucleating ice may be reached more quickly than full deliquescence of the organic phase. The full deliquescence of the organic phase is governed by condensed phase diffusion processes that may occur at longer time scales compared to ambient gas-phase RH changes. In other words, observation of heterogeneous ice nucleation by amorphous SOA in this study (simulating slow updrafts and thus slower increases in RH) will also imply heterogeneous ice nucleation to proceed for cloud systems with faster updrafts. However, no detection of SOA particles acting as IN in our experiments, does not generally rule out ice formation by SOA particles at faster updrafts.

2.6 Numerical diffusion model

The numerical diffusion model is based on the kinetic multi-layer model for gas-particle interactions in aerosols and clouds, KM-GAP.⁸⁰ KM-GAP consists of multiple model compartments and layers, namely: gas phase, near-surface gas phase, sorption layer, surface layer, near-surface bulk, and a number of bulk layers. The following processes considered in KM-GAP are relevant for this study: gas-phase diffusion, reversible adsorption, surface-to-bulk transfer, and bulk diffusion. The bulk layers can grow or shrink due to water uptake or evaporation, respectively. Mass fluxes from the far-surface into the near-surface gas phase, onto the particle surface, as well as into and between bulk layers are coupled in flux-based differential equations. A detailed description of the kinetic model can be found in Berkemeier *et al.* (2014).¹⁹

The model mimics the experimental conditions in temperature and RH and predicts the chemical composition as a function of time and depth below the particle surface. The equilibrium composition was calculated through a water activity (a_w) parameterization that translates ambient RH into equilibrium mass fractions of the bulk constituents. Sulfate containing SOA particles were assumed to be well-mixed, where inorganic sulfate depresses glass transition temperatures and increases hygroscopicity as previously shown by Saukko *et al.* (2011).²⁶ Coated soot particles were approximated as spherical core-shell structures containing a chemically inert and water-impenetrable soot core. Bulk diffusion coefficients of water molecules were estimated as a function of RH and O/C using a semi-empirical method that extrapolates the properties of the SOA surrogate sucrose²⁴ and SOA from various precursors based on properties of marker components typically found in these SOA.¹⁹ The substance-specific model input parameters are displayed in Tables 1–3. The hygroscopicity parameters (κ) were taken from Lambe *et al.* (2011).¹¹⁰ For SOA-sulfate particles, κ was estimated alongside particle density ρ , by assuming volume additivity of the pure organic and inorganic constituents' properties.¹¹⁰

In each model run, the water uptake of a single particle is simulated, following a prescribed trajectory in temperature and RH. Following the laboratory experiments, a constant temperature gradient was applied and RH calculated by assuming a constant T_d . The model yields FDRH and quasi-equilibrium T_g as functions of initial temperature, particle size, composition and humidification rate. T_g is calculated from the glass transition temperatures of the pure organic mixture, $T_{g,org}$, and that of water, $T_{g,w} = 136$ K, using a mass-based, binary Gordon–Taylor approach with a single coefficient, k_{GT} .^{20,23} At full deliquescence no glassy material remains in the organic particle and the innermost model layer is in equilibrium with the particle's gas surroundings.

Simulated T_g and FDRH can lead to four different ice nucleation regimes or scenarios:¹⁹ (1) ice formation observed at temperatures and RH below the predicted T_g may be due to ice nucleation on the solid organic particle, *i.e.* deposition ice nucleation; (2) when ice forms above T_g but below FDRH, the condensed phase organic material may be partially deliquesced with a residual solid core coated by a liquid shell and freezing proceeds *via* the immersion mode; (3) when the temperature and RH are above T_g and FDRH, respectively, only homogeneous freezing is expected due to the lack of a solid ice nucleus; (4) if ice does not form heterogeneously at low temperatures, homogeneous freezing may be suppressed

Table 3 Simulation parameters for the derivation of T_g and FDRH for biogenic and anthropogenic SOA particles for different updraft velocities. The oxygen-to-carbon (O/C) ratio is a measurable surrogate of the SOA oxidation level. ρ is particle density, κ represents the hygroscopicity parameter. $k_{GT,org}$ and $k_{GT,sulph}$ are the Gordon–Taylor coefficients for the organic and sulfate phase, respectively. T_g is the glass transition temperature of the SOA under dry conditions

Precursor	α -Pinene	α -Pinene + SO ₂	Isoprene	Isoprene + SO ₂	Naphthalene	Naphthalene + SO ₂
O/C	0.5	0.5	0.8	0.8	0.5	0.5
Organic-to-sulfate ratio	0	2	0	2	0	2
Diameter (μm)	0.2	0.2	0.2	0.2	0.2	0.2
Model layers	333	333	333	333	333	333
ρ (g cm^{-3}) ^a	1.4	1.52	1.4	1.52	1.4	1.52
κ ^b	0.213	0.252	0.174	0.291	0.12	0.252
$k_{GT,org}$ ^c	2.5	2.5	2.5	2.5	2.5	2.5
$k_{GT,sulph}$ ^e	0	4.33	0	4.33	0	4.33
T_g (K) ^d	311.7	262.5	287.2	268.8	313.1	287.6
Humidification rate (K min^{-1})	0.01; 0.1; 1	0.01; 0.1; 1	0.01; 0.1; 1	0.01; 0.1; 1	0.01; 0.1; 1	0.01; 0.1; 1
Updraft velocity ^f (m s^{-1})	0.03; 0.28, 2.8	0.03; 0.28, 2.8	0.03; 0.28, 2.8	0.03; 0.28, 2.8	0.03; 0.28, 2.8	0.03; 0.28, 2.8

^a Berkemeier *et al.* (2014).¹⁹ ^b Lambe *et al.* (2011).¹¹⁰ ^c Zobrist *et al.* (2008); Berkemeier *et al.* (2014).¹⁹ ^d Zobrist *et al.* (2008);²³ Koop *et al.* (2011).²⁰ ^e Assuming $\Gamma = 6 \text{ K km}^{-1}$.

by the presence of the glassy phase state since negligible aqueous solution is present to freeze.

3 Results and discussion

3.1 Particle phase and mixing state of SOA and SOA-soot particles

Fig. 1 displays the SEM images of representative biogenic SOA with and without the presence of sulfate recorded with a magnification ranging from 12 000 to 35 000. These images reveal remarkable differences in particle phase states during particle generation conditions at room temperature and at $\sim 30\%$ RH. Although the impaction stages were rotated, aerosol number concentrations and collection times were sufficiently high for collision of deposited particles to occur on the substrate. Further, there is evidence for the coalescence of some SOA particles. Coalescence events are identified by the presence of different sizes of deposited particles rather than a uniform particle size distribution arising from the cut-point diameter of the impaction stage. SEM images with particles residing close to one another or in contact to each other indicate negligible coalescence upon collision. Thus, the extent of coalescence events observed for different SOA types is a qualitative indicator of particle viscosity. Fig. 1 shows that compared to α -pinene and isoprene SOA, which appear more liquid-like (some coalescence),

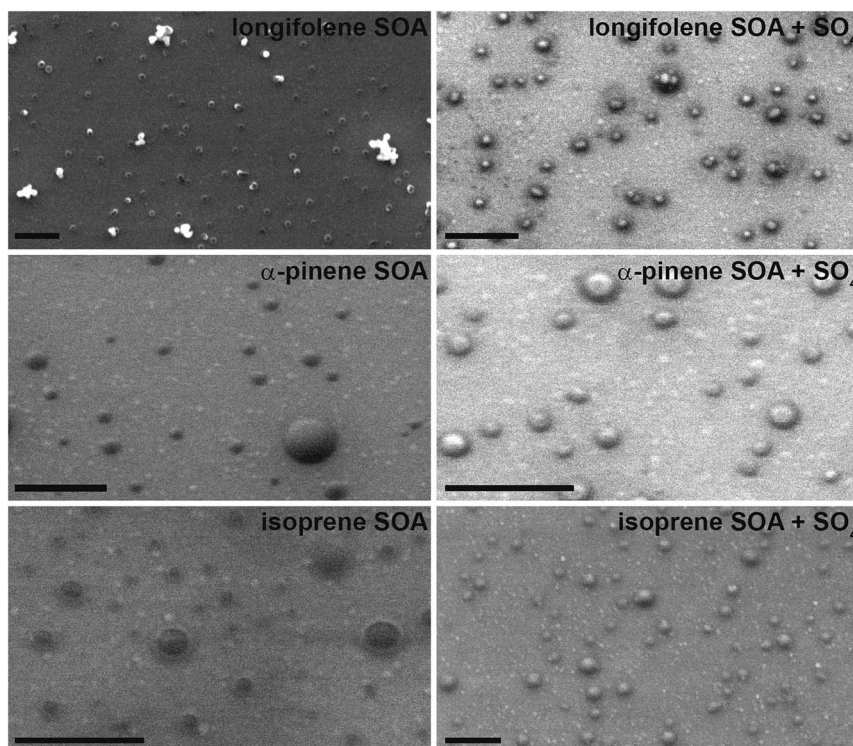


Fig. 1 Scanning electron microscope images of deposited longifolene, α -pinene, and isoprene SOA with and without the presence of sulfates using stage 8 (cut-point of 180 nm) of the impactor. Scale bars represent 1 μm and vary in size due to differences in applied magnification.

longifolene SOA particles did not coalesce upon impaction onto the substrate. Coalescence of deposited longifolene SOA particles does occur upon mixing with sulfate due to the plasticizing effect of liquid water associated with the sulfate. Overall, the observed trends in particle phase state qualitatively agree with the measured phase state dependent particle bounce fractions.²⁶

STXM/NEXAFS analysis was performed to map organic carbon functionality and inorganic material within the biogenic SOA particles. Fig. 2 shows X-ray

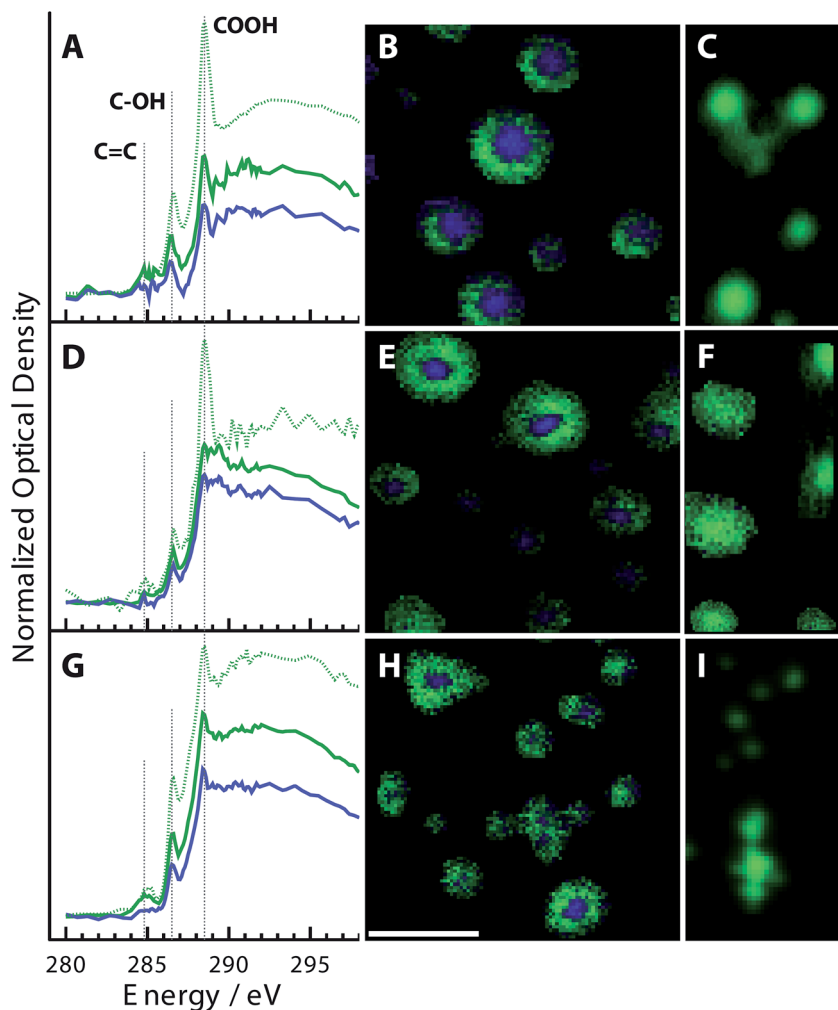


Fig. 2 STXM/NEXAFS analyses of α -pinene (A, B, C), isoprene (D, E, F), and longifolene (G, H, I) SOA particles. X-ray absorption spectra are shown in A, D, and G as normalized and averaged optical density as a function of energy. Vertical dotted lines appear at 284.8, 286.5 and 288.5 eV indicating absorption peaks that reflect carbon double bonding, alcohol, and carboxyl functionalities, respectively. Solid green and blue spectra are derived from SOA particles containing sulfate (B, E, H) while dotted green spectra are derived from SOA particles without sulfate (C, F, I). Representative component SOA particles with sulfate are shown in component images B, E and H while particles without sulfate are shown in C, F, and I. The scale bar for all images is 1 μm and is shown in panel H.

absorption spectra and representative component images of the investigated SOA particle types. Absorption of X-rays at a given energy is reported as an optical density (OD). The spectra displayed in Fig. 2 were first normalized to their integrated area and then spectra for 10–40 particles were averaged. Thus, the spectra in Fig. 2A, D, and G are presented as normalized OD. This has the advantage that small and large particles contribute equally to the calculated average and the ratios between peak-heights and the post- and pre-edge are preserved. Component maps and spectra were generated employing specific thresholding requirements described by Moffet *et al.* (2010).¹⁰³ For example, the core of a SOA particle with sulfate typically satisfies the requirement that the ratio between the pre-edge OD (278 eV) and post-edge OD (320 eV) be greater than half, *i.e.* $OD_{\text{pre}}/OD_{\text{post}} > 0.5$.¹⁰³ Therefore, most of the particle cores presented in Fig. 2B, E and H are labelled as having a dominating inorganic component shown in blue. Particle edges are dominated by the carboxyl functionality and are shown in green.

Similar organic carbon functionalities for all biogenic SOA particles were observed. This can be seen by the identical dominant absorption peaks occurring at 288.5 and 286.5 eV indicating carboxyl and alcohol functional groups.⁷⁷ Beam damage on these particles was assessed and under conditions where it was observed, OD increased at 284.8 eV and decreased at 286.5 and 288.5 eV. The spectra in Fig. 2 were acquired under conditions where beam damage was not significantly observed. The absorption peak height ratios were dissimilar among

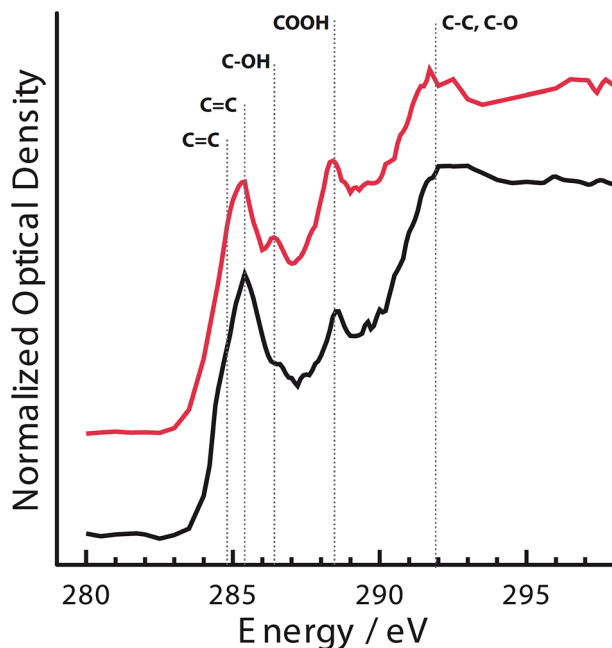


Fig. 3 STXM/NEXAFS spectra of soot coated with α -pinene (red) and naphthalene (black) SOA. X-ray absorption spectra are normalized and averaged and represent optical density as a function of energy. Vertical dotted lines indicate major absorption peaks located at 284.8, 285.4, 286.5, 288.5 and 291.9 eV. The spectra are vertically shifted for better visualization.

SOA particles from different chemical precursors. This may be indicative of different O/C ratios (Table 1), *e.g.*, α -pinene SOA shown in Fig. 2 had O/C = 0.74 resulting in a more pronounced carboxyl peak compared to longifolene SOA with O/C = 0.45. Differences in peak heights may also be related to different gas phase oxidant chemistry producing low-volatility compounds with unique functionalities.

Absorption spectra of soot particles coated with either α -pinene or naphthalene SOA are shown in Fig. 3. A clear dominating spectral feature is the absorption peak at 285.4 eV, common for atmospheric soot.^{76,95} An absorption shoulder at around 284.8 eV indicates C=C associated with quinones.⁷⁷ A second well-defined peak at 288.5 eV indicates the carboxyl functionality. The carboxyl and alcohol absorption peaks are located at the same X-ray energies for soot coated with α -pinene SOA, soot coated with naphthalene SOA, and the biogenic SOA (Fig. 2). The broad absorption plateau at X-ray energies \sim 292 eV is indicative of the σ^* electronic transition for C*-C and C*-O. We note that the spatial resolution of STXM is very similar to the SOA coating thicknesses (Table 2). Thus, spatial identification of organic coatings was at the detection limit of the X-ray microscope. However, it was observed that the carboxyl absorption peak was observed over the entire particle, providing qualitative evidence of a uniform organic coating.

Since none of the biogenic and anthropogenic precursor gases possess oxygenated functional groups, the appearance of carboxyl and alcohol groups provides evidence of oxidation as expected from the photochemical production of SOA.^{9,111,112}

3.2 Heterogeneous ice nucleation by SOA particles

3.2.1 Longifolene SOA particles. Fig. 4 shows observed ice formation events for longifolene SOA with and without the presence of sulfate. Longifolene SOA did not nucleate ice at temperatures above the homogeneous freezing limit. Furthermore, water uptake was only observed close to water saturation. For $T_p < \sim$ 235 K, longifolene SOA formed ice at conditions expected for homogeneous freezing. Although longifolene SOA particles are highly viscous (see Fig. 1), the experimental data suggest that these particles readily deliquesce upon increasing RH and thus behave like aqueous droplets with regard to ice nucleation. At temperatures above the homogeneous freezing limit, longifolene SOA with sulfate take up water at lower RH_{ice} compared to longifolene without sulfate. The phase state of longifolene SOA with sulfate at the point of visible water uptake is unclear. STXM analysis shows that these particles exhibit a core-shell configuration at particle collection conditions, though one would expect liquid-liquid phase separation at \sim 93% RH at room temperature.¹¹³ At lower temperatures, longifolene SOA with sulfate form ice at conditions expected for homogeneous ice nucleation. As shown in Fig. 4, the longifolene SOA particles exhibit homogeneous ice nucleation efficiencies similar to aqueous sulphuric acid particles. These results suggest that the ice nucleation potential of these biogenic SOA particles can be represented by the a_w based homogeneous ice nucleation theory.¹¹⁴⁻¹¹⁶ Hence under mixed-phase cloud conditions, longifolene SOA particles most likely do not play a major role in cloud glaciation processes. However, the presence of small amounts of inorganic species increases particle

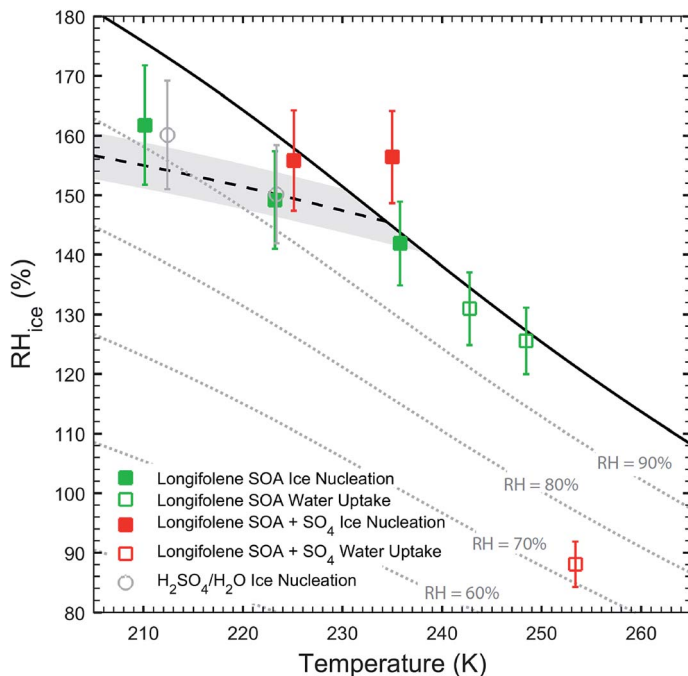


Fig. 4 Thermodynamic conditions at which longifolene SOA particles with (red) and without (green) sulfate initiate water uptake and ice formation. Filled and open symbols represent freezing and water uptake, respectively. Ice formation by aqueous H_2SO_4 particles is shown by open grey circles. The dashed black line represents the homogeneous freezing limit for $J_{\text{hom}} \approx 10^{10} \text{ cm}^{-3} \text{ s}^{-1}$ including $\Delta a_w = \pm 2.5$ given by the grey shaded region,^{115,116,133} and the solid black line indicates water saturation (100% RH).¹⁰⁴ Dotted grey lines represent constant RH.

hygroscopicity significantly.^{117–120} This may facilitate the formation of supercooled liquid droplets even at temperatures as low as 254 K (when neglecting other competing effects).

3.2.2 α -Pinene SOA particles. Fig. 5 shows observed ice formation events for α -pinene SOA. For temperatures above the homogeneous freezing limit, α -pinene SOA particles do not initiate freezing. Water uptake occurs at a significantly lower RH compared to the longifolene SOA particles, supporting the qualitative findings of a more liquid-like phase as inferred from the SEM images. The presence of sulfate has only a minor effect on water uptake by α -pinene SOA particles, decreasing observed uptake by ~ 5 –10% RH_{ice} . α -pinene SOA particles with sulfate exhibit a core-shell configuration as indicated by STXM (Fig. 2). Thermodynamically, these particles may undergo liquid-liquid phase separation at $\sim 45\%$ RH.¹¹³ It is not clear if phase separation has a significant effect on the observed reduction in water uptake threshold RH. For temperatures as low as 248 K, water uptake is observed at 88–100% RH_{ice} (*i.e.* 77–80% RH), whereas for $T_p < 240$ K, water uptake occurs at 131% RH_{ice} . For $T_p < 236$ K, α -pinene SOA particles form ice at conditions typical for homogeneous ice nucleation. The data suggest that α -pinene SOA particles do not significantly impact ice crystal formation under mixed-phase cloud conditions. Recently, Lienhard *et al.* (2015)²⁹ determined water diffusion

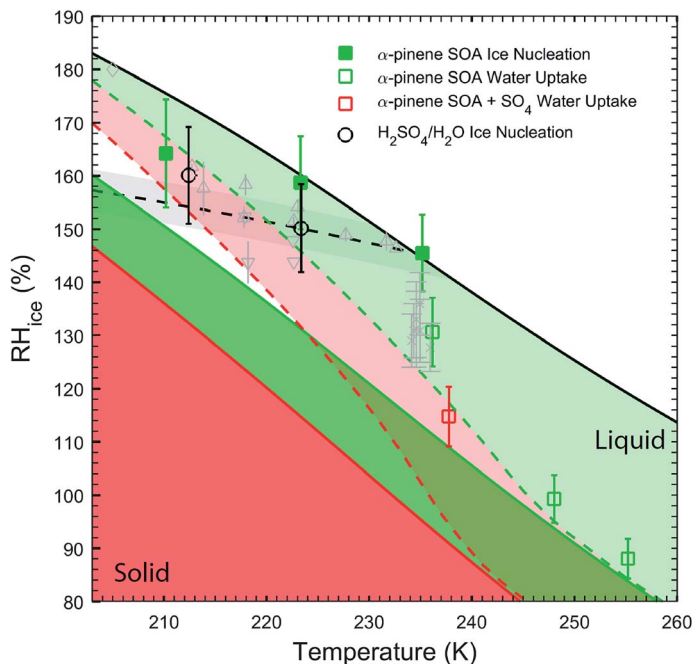


Fig. 5 Thermodynamic conditions at which α -pinene SOA particles with (red) and without (green) sulfate initiate water uptake and ice formation. Filled and open symbols represent freezing and water uptake, respectively. Ice formation by aqueous H_2SO_4 particles is shown as open black circles. The corresponding simulated glass transition temperatures are given by the respective solid lines and the corresponding FDRH are given by the dashed lines. Darker shading corresponds to respective solid (glassy) SOA regime (*i.e.* below T_g) and brighter shading corresponds to respective liquid regime (above FDRH). The ice nucleation data by Möhler *et al.* (2008)⁵² is shown as a diamond, by Ladino *et al.* (2014)⁵¹ as triangles and as downward pointing triangles indicating pre-cooled particles, and by Ignatius *et al.* (2016)⁵⁰ as crosses. The solid and dashed black (with grey shading) lines are the same as in Fig. 4.

coefficients in α -pinene SOA particles. Their study suggests that only at temperatures below 220 K and under fast updraft velocities, heterogeneous ice nucleation may occur in the immersion mode on glassy α -pinene SOA cores. This is supported by our experimentally obtained ice nucleation data depicted in Fig. 5.

For comparison, previous ice nucleation data of α -pinene SOA are plotted in Fig. 5. The α -pinene SOA applied in the other studies were generated by O_3 oxidation of α -pinene at room temperature, except in the study by Ignatius *et al.* (2016)⁵⁰ where temperatures ranged from 235.15 K to 263.15 K. Möhler *et al.* (2008)⁵² and Ladino *et al.* (2014)⁵¹ found that α -pinene SOA forms ice at or above the homogeneous freezing limit. Ladino *et al.* (2014)⁵¹ did not observe changes in O/C from 0.39 to 0.78 to impact ice nucleation significantly. However, when the SOA particles were pre-cooled, nucleation occurred for RH_{ice} lower than expected for homogeneous freezing. Ignatius *et al.* (2016)⁵⁰ observed heterogeneous ice nucleation by α -pinene SOA particles with O/C = 0.25 at ~ 235 K. As discussed in the following section, a lower O/C of α -pinene SOA is expected to result in T_g and FDRH being lower with respect to temperature and RH_{ice} and thus decreasing the

particles' ability to act as IN. The observation of heterogeneous freezing by these α -pinene SOA particles may be due to the different chemical composition of the SOA particles or due to the short ice nucleation activation time of 10 s which may yield only partially deliquesced particles providing a substrate for nucleation to occur.

The simulated T_g for α -pinene SOA is significantly higher with respect to RH_{ice} compared to the T_g for α -pinene SOA with sulfate, clearly indicating the role of sulfate and associated water on particle viscosity (Fig. 5). Except for the freezing points at the lowest observed temperature, all freezing and water uptake occurs at RH_{ice} above FDRH, corroborating the numerical diffusion model. At 210 K, α -pinene SOA particles form ice at the homogeneous freezing limit which reflects conditions where the particles become more liquid-like as they transition from T_g to FDRH. At 210 K, homogeneous ice nucleation is predicted to occur in an aqueous solution with $a_w \approx 0.88$.¹¹⁵ Assuming equilibrium between the SOA particles and chamber RH, the observed freezing occurs in this expected a_w range with a mean value slightly above $a_w \approx 0.9$ (Fig. 5). This implies that the remaining highly viscous SOA particle does not contribute to ice nucleation. The presence of sulfate reduces simulated FDRH by a similar degree as the difference in observed water uptake for SOA particles with and without sulfate as evident at ~ 237 K (Fig. 5). Overall, the diffusion model correctly captures the observed trend of water uptake by α -pinene SOA with and without sulfate.

3.2.3 α -Pinene SOA coated soot particles. Fig. 6 shows the conditions of the first ice formation events by α -pinene SOA-coated soot particles with O/C = 0.42–0.45 (medium O/C) and 0.59–0.64 (high O/C), SOA coating thicknesses of 9–30 nm (low coating thickness) and 66–68 nm (high coating thickness). For $T_p > 229$ K, these mixed SOA/soot particles formed ice *via* immersion freezing at 229 and 239 K at water saturation independent of O/C and SOA coating thickness. However, at 229 K, the possibility of homogeneous ice nucleation cannot be ruled out. For soot acting as IN, its nucleation rate ($\omega_{soot} = J_{het}^{soot} \times S^{soot}$) must be greater than the homogeneous ice nucleation rate ($\omega_{hom} = J_{hom} \times Vol$), *i.e.* $J_{het}^{soot} > J_{hom}(230 \text{ K}, 152\% RH_{ice})^{115} \times Vol/S^{soot}$. Assuming 1 μm hemispheric droplets, soot cores with ~ 164 nm diameter, and $N \approx 60\,000 \text{ mm}^2$ (Table 1), we estimate $J_{het}^{soot} > 10^{16} \text{ cm}^{-2} \text{ s}^{-1}$. J_{het}^{soot} values depend on soot type and coating and are not readily available. For example, Dymarska *et al.* (2006)⁶⁵ estimated that for uncoated soot, $J_{het} = 50 \text{ cm}^{-2} \text{ s}^{-1}$. Under our experimental conditions, it is very likely that homogeneous ice nucleation dominates. This observation is in agreement with a study by Kulkarni *et al.* (2016).⁷³ They found that after ageing for several hours (presumably resulting in high O/C), soot particles coated with α -pinene formed ice at the homogeneous freezing limit for temperatures between 223 K and 233 K as shown in Fig. 6. At 239 K and water saturation (*i.e.* $RH = 100\%$ or $a_w = 1$), ice nucleation is likely due to the presence of soot particles. This is because, $J_{hom}(240 \text{ K}, a_w = 1) \approx 237 \text{ cm}^{-3} \text{ s}^{-1}$ (ref. 115) and assuming that $N \approx 60\,000$, hemispheric water droplets 1 μm in diameter result in $\omega_{hom} = 3 \times 10^{-5} \text{ s}^{-1}$ or one ice nucleation event in ~ 9 h. Furthermore, as discussed above, α -pinene SOA without soot did not form ice at $T_p > 235$ K (Fig. 5). Chou *et al.* (2013)⁵⁹ observed photochemically aged diesel particles coated with α -pinene SOA to form ice above water saturation at 238 K. It is not clear if ice formation was initiated by homogeneous or heterogeneous freezing. At $T_p < 220$ K, the particles nucleated ice at mean RH_{ice} values ranging from 137 to 156% between 210 and 220 K. The data indicate that

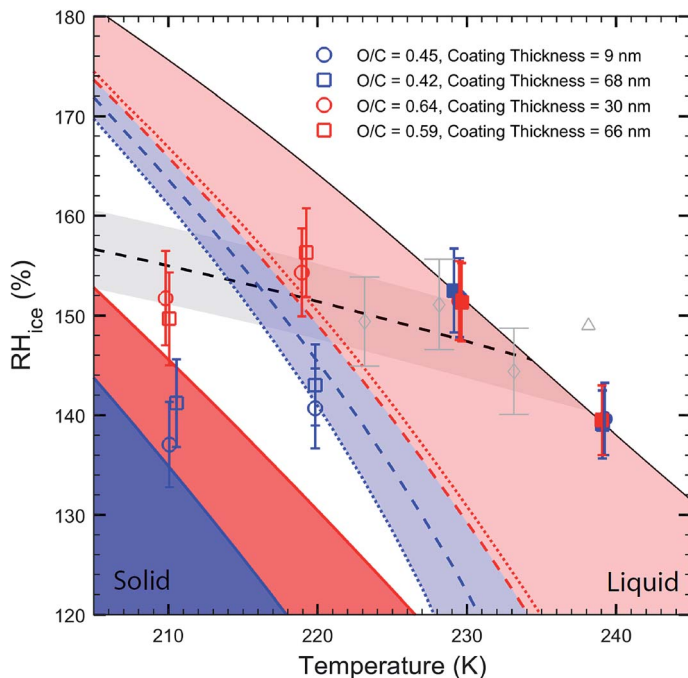


Fig. 6 Thermodynamic conditions at which α -pinene SOA coated soot particles for $O/C \approx 0.42$ – 0.45 (blue) and $O/C \approx 0.59$ – 0.65 (red) initiate ice formation. The circles correspond to low coating thickness of 9–30 nm and the squares represent high coating thickness of 66–68 nm (Table 2). Filled and open symbols represent immersion freezing and deposition ice nucleation, respectively. The corresponding T_g is given by the respective solid lines, and the corresponding FDRH are given by the dotted (low coating thickness) and dashed (high coating thickness) lines. Darker shading corresponds to a respective solid (glassy) SOA regime (*i.e.* below T_g) and brighter shading to a respective liquid regime (above FDRH). The ice nucleation data by Chou *et al.* (2013)⁵⁹ is shown as a triangle and the data by Kulkarni *et al.* (2016)⁷³ as diamonds. The solid and dashed black (with grey shading) lines are the same as in Fig. 4.

the SOA oxidation level influences the temperature and RH_{ice} at which ice nucleation occurs. α -Pinene SOA coated soot particles with $O/C \approx 0.59$ – 0.65 form ice at the homogeneous freezing limit ($RH_{ice} \approx 154\%$), in agreement with previous findings.⁷³ However, soot particles with SOA coating of $O/C \approx 0.43$ initiated ice formation at $RH_{ice} \approx 142\%$. SOA coating thickness does not play a significant role in ice formation conditions over the range of coating thicknesses surveyed in these measurements.

The numerical simulation suggests that, on average, for typical mixed-phase cloud conditions the SOA material is completely deliquesced (*i.e.* $T_p > \sim 232$ K, $RH_{ice} = 120\%$, Fig. 6). However, ice formation occurred at water saturation at 239 K implying that a highly diluted aqueous solution, or water, is present. Presumably, freezing is initiated by the presence of the immersed insoluble soot particles. At 220 K the SOA coated soot particles with $O/C \sim 0.4$ formed ice at, or slightly below, RH_{ice} of the respective FDRH lines while SOA coated soot particles with $O/C \sim 0.6$ formed ice at RH_{ice} only above expected FDRH. This suggests that soot

particles coated with less-oxidized α -pinene SOA nucleated ice while in a semi-solid state, while soot particles coated with more oxidized α -pinene SOA formed ice while in a more liquid-like phase. Although the model suggests that ice formation proceeded from both semisolid and liquid particles, *i.e.* the particles acquired water, the data are categorized as deposition ice nucleation. The expected minor water uptake²⁷ cannot be verified with the limited resolution of our instrumentation.⁹³ Future nanoscale observation of ice nucleation may allow for the examination of the actual underlying nucleation pathway.¹²¹ At 210 K the SOA coated soot particles form ice at, or slightly above, their respective T_g and below their FDRH. For these reasons the SOA coating of the particles likely exhibits a highly viscous phase that allows for heterogeneous ice nucleation. We hypothesize that at or just above T_g , the organic matrix remains sufficiently viscous to provide a substrate to initiate ice nucleation while maintaining sufficient flexibility to allow for the movement of potential bonding sites (*e.g.* by hydrogen bonds) to accommodate the embryonic ice crystal. This is indirectly supported by a recent study which shows that liquid organic IN can initiate ice nucleation.¹²²

3.2.4 Naphthalene SOA coated soot particles. Fig. 7 shows the conditions of the first ice formation events by naphthalene SOA coated soot particles with O/C = 0.40–0.44 (medium O/C) to 1.03 (high O/C), and SOA coating thicknesses from 53 (low coating thickness) and 76 (high coating thickness) nm. These particles formed ice *via* immersion freezing mode at water saturation at ~ 239 K and at $\text{RH}_{\text{ice}} \approx 147\%$ at 230 K independent of O/C and SOA coating thickness. At 230 K, the naphthalene SOA coated soot particles formed ice below water saturation in the range of the expected homogeneous freezing limit. At $T_p < 229$ K, the particles nucleated ice in the deposition mode at mean RH_{ice} values ranging from 140% to 152% between 210 and 220 K. At ~ 220 K, naphthalene SOA coated soot particles with medium O/C formed ice at conditions similar to homogeneous freezing. However, naphthalene SOA coated soot particles with high O/C formed ice at lower RH_{ice} making them more efficient IN. The ice formation trend for naphthalene SOA coated soot particles is opposite to the one of α -pinene SOA coated soot particles with regard to O/C. This may reflect the opposing trend in T_g with O/C between the two SOA types, where the higher O/C of naphthalene SOA results in a lower T_g (Fig. 7) and the higher O/C of α -pinene SOA yields a higher T_g compared to SOA particles with a medium O/C (Fig. 6). At 210 K, no significant effect of particle oxidation level on ice nucleation was observed. Over the range of SOA coating thicknesses examined, the coating thickness appears to play an insignificant role in modifying the ice formation conditions.

The numerical diffusion model suggests that at 210 K, the naphthalene SOA coated soot particles nucleated ice below their respective T_g , indicating that the SOA coating existed as an amorphous solid and thus could act as IN, corroborated by experiments. At 220 K, the particles nucleated ice at RH_{ice} above their respective T_g and below their FDRH, which indicates that the SOA coating existed in a semisolid state, allowing for heterogeneous ice nucleation. This may rule out the apparent homogeneous nucleation process of SOA coated particles with a medium O/C at $\text{RH}_{\text{ice}} \approx 154\%$. The potential presence of semisolid organic material in these SOA coated particles with a high and medium O/C at ~ 220 K may imply the negligible influence of the soot core acting as IN. At ~ 230 K and ~ 239 K, the particles formed ice above the respective FDRH, suggesting that

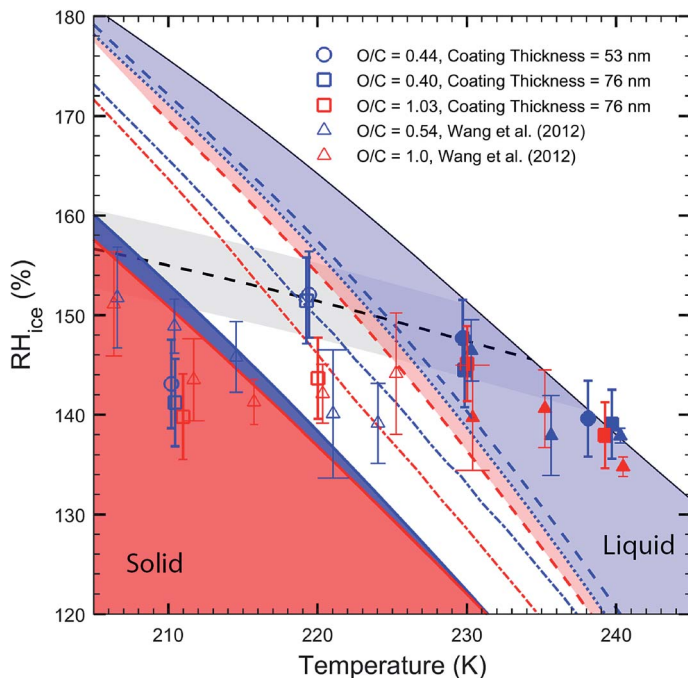


Fig. 7 Thermodynamic ice nucleation conditions by naphthalene SOA coated soot particles for $O/C \approx 0.40$ – 0.44 (blue) and $O/C \approx 1.03$ (red). The circles correspond to a low coating thickness of 53 nm and the squares represent a high coating thickness of 76 nm (see also Table 2). Filled and open symbols represent immersion freezing and deposition ice nucleation, respectively. The corresponding simulated T_g is given by the solid lines, and respective FDRH are given by the dotted (low coating thickness) and dashed (high coating thickness) lines. Darker shading corresponds to the respective solid (glassy) SOA regime (*i.e.* below T_g) and brighter shading to the respective liquid regime (above FDRH). Triangles represent ice nucleation data by naphthalene SOA particles with $O/C \approx 0.54$ (blue) and $O/C \approx 1.0$ (red), where open triangles indicate deposition ice nucleation and closed triangles immersion freezing,³¹ and corresponding FDRH¹⁹ are given as dot-dashed lines. The solid and dashed black (with grey shading) lines are the same as in Fig. 4.

a liquid SOA coating surrounds the soot core. The coincidence of ice formation at ~ 230 K with the expected homogeneous freezing ($RH_{ice} \approx 146\%$) may imply that the soot particle does not significantly impact ice nucleation under these conditions. In the absence of other insoluble material, freezing at ~ 239 K may only be explained by the presence of soot particles acting as IN since J_{hom} is too small. However, when considering previous ice nucleation data of naphthalene SOA by Wang *et al.* (2012),³¹ remaining highly viscous condensed phase organic material acting as IN cannot be ruled out.

For comparison, Fig. 7 includes the ice nucleation data by Wang *et al.* (2012)³¹ and associated simulations by Berkemeier *et al.* (2014)¹⁹ for naphthalene SOA particles with different O/C ratios with no soot present. Wang *et al.* (2012)³¹ observed deposition ice nucleation occurring over similar temperature and RH_{ice} conditions as in the present study (except at 205 K and some data points at 220 K). At T_p of ~ 236 K and ~ 240 K, Wang *et al.* (2012)³¹ observed immersion freezing at

conditions at which the model suggests naphthalene SOA particles are fully deliquesced. However, the numerical diffusion model does not consider insoluble oxidation products that can remain in the aqueous phase.¹⁹ If this would be the case, this would imply that the freezing of ice observed in this study at 239 K may not be due to immersed soot particles but could also be due to the remaining solid organic material acting as IN. At 230 K, it is not entirely clear which particle constituent initiates ice formation: the aqueous phase, the soot core, or some remaining highly viscous organic material. However, considering that $J_{\text{hom}}(230 \text{ K}, a_w = 0.96) \approx 10^9 \text{ cm}^{-3} \text{ s}^{-1}$, homogeneous ice nucleation may provide the fastest pathway for ice formation.

4 Atmospheric implications

We apply the numerical diffusion model to estimate T_g and FDRH for biogenic and anthropogenic SOA with and without sulfate for typical⁹ particle O/C, organic-to-sulfate ratios, and different atmospheric updraft velocities as given in Table 3. Fig. 8 shows these simulation results for isoprene SOA, α -pinene SOA, and naphthalene SOA.

Isoprene SOA exhibits T_g and FDRH that are lowest in temperature and RH_{ice} compared to the other simulated biogenic SOA types. Fig. 8a demonstrates that a change of two orders of magnitude in updraft velocity changes the FDRH significantly. Also, the presence of sulfate decreases the corresponding FDRH substantially with respect to temperature and RH_{ice} , as sulfate can act as a plasticizer. For typical mixed-phase cloud conditions ($T > \sim 235 \text{ K}$) isoprene SOA particles likely fully deliquesce before initiating heterogeneous ice nucleation. However, for temperatures below 235 K, isoprene SOA particles can potentially act as IN since relatively high RH can be reached before full deliquescence occurs. When sulfate is present, heterogeneous ice nucleation may only be possible at temperatures below $\sim 220 \text{ K}$. In the absence of laboratory ice nucleation data, the importance of isoprene SOA for cirrus formation cannot be ruled out. However, assuming that isoprene SOA exhibits similar ice nucleation propensities as the investigated α -pinene and longifolene SOA (Fig. 4 and 5), its significance in serving as IN for cirrus formation may be minor.

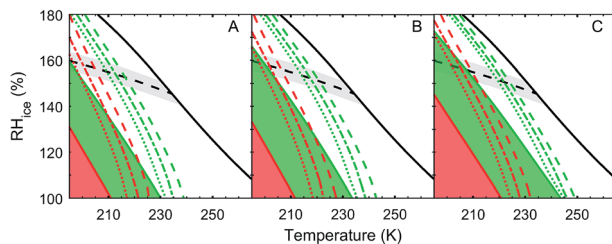


Fig. 8 Simulated T_g and FDRH for isoprene (A), α -pinene (B), and naphthalene (C) SOA with (red) and without sulfate (green) for different updraft velocities for parameters given in Table 3. Solid green and red lines represent respective T_g . The shading corresponds to respective solid (glassy) SOA regime (*i.e.* below T_g). Dotted, dash-dotted, and dashed lines represent FDRH for updrafts of 0.03, 0.28, and 2.8 m s^{-1} , respectively. The solid and dashed black (with grey shading) lines are the same as in Fig. 4.

Fig. 8b displays simulation results for α -pinene SOA, which has a slightly higher T_g and FDRH compared to isoprene SOA. Similar to isoprene SOA, changes in updraft velocity or addition of sulfate can have a significant impact on the particle phase state and in turn on the particles' ability to act as IN. The simulation results are consistent with our experimental observations that α -pinene SOA with and without sulfate do not act as IN under mixed-phase cloud conditions. Only at temperatures below ~ 238 K, α -pinene SOA can act as IN, although this is not observed in our experiments. These findings may indicate that, although α -pinene SOA may be present in an amorphous solid or semisolid, it may not represent a very active IN. However, the oxidation level of α -pinene SOA particles can have a significant effect on the particles' T_g and FDRH, where a higher O/C leads to T_g and FDRH to occur at higher temperatures and RH_{ice} (Fig. 6). In the presence of sulfate, temperatures have to be lower than ~ 222 K to sustain an amorphous solid or semisolid phase potentially acting as IN (Fig. 8b). For lower temperatures, thermodynamic considerations allow the existence of semisolid and solid α -pinene SOA phases, which, however, do not result in ice formation at RH_{ice} below the homogeneous freezing limit as inferred from our experiments. This suggests a negligible role of α -pinene SOA to act as IN under cirrus formation.

The experimental water uptake and ice nucleation data of longifolene SOA with and without sulfate follow the observed trends for α -pinene SOA particles. Longifolene SOA with and without sulfate do not induce ice nucleation for temperatures above the homogeneous freezing temperature and thus are likely not important for mixed-phase cloud formation. The presence of sulfate significantly reduces the observed water uptake onset. At temperatures below ~ 238 K, longifolene SOA with and without sulfate nucleated ice at the homogeneous freezing limit indicating little propensity to act as IN. These experimental observations suggest that longifolene SOA with and without sulfate does not play a substantial role as IN in the atmosphere but likely participates in cloud glaciation *via* homogeneous freezing.

In general, the presence of sulfate in the organic matrix yields a greater association with water acting as a plasticizer, which in turn significantly lowers T_g and FDRH.²⁰ When associating the presence of sulfate in biogenic SOA with anthropogenic activities, as a consequence, the heterogeneous ice nucleation capability of biogenic SOA is rendered less important, even for upper tropospheric temperatures typical of cirrus formation. Our study suggests that for current time periods the atmospheric ice nucleation relevance of biogenic SOA for temperatures below ~ 238 K could be diminished compared to pre-industrial times and pristine areas devoid of high sulfate concentrations such as the Amazonian region. However, in the case of α -pinene SOA, increases in particle oxidation level can increase T_g and FDRH. Hence, highly oxidized biogenic SOA particles stemming from a photochemically active environment or being chemically aged during atmospheric transport^{123–126} may more effectively act as IN. This may be important when simulating conditions relevant to pre-industrial times and thus warrants further investigation. Note that sulfate–SOA mixed particles in ambient conditions may be phase-separated especially when the O/C of SOA materials is low.¹²⁷ In case of a core–shell morphology with an inorganic-rich phase as the core and an organic-rich phase as the shell, both phases would take up water according to their different hygroscopicities and water molecules would diffuse

through the organic shell to reach the inorganic core.¹²⁸ These effects and interplay of phase state, phase separation, and morphology on heterogeneous ice nucleation need to be further investigated in experiments and model simulations.

Naphthalene SOA is characterized by the highest T_g and FDRH (Fig. 8c) among the SOA types that were studied. Furthermore, the diffusion model results demonstrate that naphthalene SOA oxidation level does not have such a significant impact on T_g and FDRH compared to the case of α -pinene SOA (Fig. 6 and 7). The model simulations suggest that naphthalene SOA can act as IN at temperatures as high as 247 K, which lies in the mixed-phase cloud regime, in agreement with experimental observations. For temperatures below ~ 230 K, our experimental and simulation results provide support for naphthalene SOA acting as IN. The presence of sulfate decreases the maximum temperature to act as IN to ~ 227 K, ruling out naphthalene SOA with sulfate playing a major role as IN under mixed-phase cloud conditions. In this case, the presence of sulfate has a much greater effect on T_g and FDRH than variation in particle oxidation state. The simulation suggests that FDRH of naphthalene SOA with sulfate are more sensitive to updraft velocity compared to naphthalene SOA which is a result of the interplay of the a_w of the surrounding aqueous solution and core viscosity.¹⁹ Overall, considering T_g and FDRH estimates and experimental ice nucleation data, naphthalene SOA can play a greater role in ice crystal formation under mixed-phase and cirrus cloud conditions compared to the investigated biogenic SOA. Anthropogenic SOA having highly viscous phase states may positively impact cloud glaciation processes when present in abundance in the atmosphere and this warrants further investigation of their formation processes and phase states. If the oxidation of aromatic SOA precursors produces insoluble organic material that in turn impacts the particle phase state and thus ice nucleation, particularly under mixed-phase cloud conditions, this warrants further investigation.

The presence of soot particles in internally mixed soot–SOA particles may be most important at temperatures typical for mixed-phase cloud conditions. Under these conditions, we found the soot particles very likely initiated immersion freezing in α -pinene SOA coated soot particles independent of O/C and coating thickness. However, for temperatures in the homogeneous freezing range, we observe ice nucleation, likely initiated by the presence of soot particles, only for temperatures below ~ 220 K and medium O/C. We hypothesize that fossil-fuel derived soot particles internally mixed with SOA may positively impact glaciation processes under mixed-phase cloud conditions compared to conditions that were prevalent in pre-industrial times.

5 Summary and conclusions

We characterized SOA particles generated from the OH oxidation of naphthalene, α -pinene, and longifolene serving as surrogates of anthropogenic and biogenic SOA particles with or without the presence of sulfate and soot particles for their role in atmospheric ice nucleation under mixed-phase and cirrus cloud conditions. A numerical diffusion model was applied to estimate the T_g and FDRH of isoprene, α -pinene, longifolene, and naphthalene SOA with or without sulfate and soot particles. Biogenic SOA particles with sulfate exhibit a core–shell structure, where a sulfate-rich domain represents the core surrounded by oxidized organic material. Soot particles possess a uniform coating of SOA material. Longifolene

SOA is the only SOA type that displays a highly viscous, potentially solid phase at ambient conditions while other biogenic SOA particles appear liquid-like. This effect is exacerbated when sulfate is present.

Ice nucleation experiments conducted at temperatures as low as 210 K and coupled numerical diffusion modelling simulations suggest that biogenic SOA with and without sulfate do not act as IN under mixed-phase cloud conditions. The solid longifolene SOA particles quickly deliquesce upon reaching their critical deliquescence RH and do not act as IN. For $T < 235$ K, α -pinene and longifolene SOA with and without sulfate do not demonstrate ice formation at RH_{ice} below that required for homogeneous ice nucleation. This is despite the fact that simulations of T_g and FDRH for α -pinene SOA suggest the presence of a highly viscous phase that potentially could nucleate ice. Model simulations further suggest that isoprene SOA does not play a major role as IN. We found that the oxidation level of α -pinene SOA can significantly change T_g and FDRH and in turn the particles' role in ice cloud formation. Considering different particle oxidation states and sulfate to organic ratios for their role in particle phase state at lower temperatures and ice formation warrants further investigation.

The presence of soot in α -pinene SOA and naphthalene SOA particles could not be unambiguously attributed to promoting ice nucleation for temperatures below ~ 235 K. For the most part, the SOA particles' ice formation potential correlates with the phase state of the SOA. Soot particles can act as IN for α -pinene SOA coated soot particles under mixed-phase cloud conditions. However, the propensity for soot acting as IN in naphthalene coated soot particles under those conditions remains ambiguous. This also implies an incomplete understanding of the condensed phase oxidation products created during the formation of SOA from aromatic precursors. Overall, naphthalene SOA is the most efficient IN among all investigated SOA types.

Though much more research is needed addressing the wide range of SOA physicochemical properties impacting ice nucleation such as oxidation level, mixing state and phase separation, we can conclude the following from this study: biogenic SOA particles likely do not play a significant role in mixed-phase cloud formation, especially when mixed with sulfate. Thus, we do not expect significantly different ice cloud formation response during pre-industrial times compared to current conditions unless the oxidative capability of the atmosphere is significantly different, thereby influencing the particle oxidation level and the corresponding phase state. To the extent that naphthalene SOA is representative of other anthropogenic SOA types, our results suggest that anthropogenic SOA may play a greater role in atmospheric ice nucleation under mixed-phase and cirrus cloud conditions compared to biogenic SOA. Soot particles coated with SOA have the most significant effect on ice formation at conditions typical for mixed-phase cloud conditions since at lower temperatures the SOA material can also provide a solid phase for ice nucleation. For these reasons, under current conditions, a higher number of immersion freezing events under mixed-phase cloud conditions may be expected compared to conditions during pre-industrial times or over pristine regions with negligible soot emissions.

Acknowledgements

This work was funded by the U.S. Department of Energy, Office of Science (BER), Atmospheric System Research (DESC0008613 and DE-SC0016370). The Boston College/Aerodyne Research co-authors acknowledge support by the Atmospheric Chemistry Program of the U.S. National Science Foundation under grants AGS-1536939, AGS-1537446 and AGS-1537009 and by the U.S. Office of Science (BER), Department of Energy (Atmospheric Systems Research) under grants DE-SC0006980 and DE-SC0011935. The STXM/NEXAFS particle analysis was performed at beamlines 11.0.2.2 and 5.3.2.2 at the Advanced Light Source (ALS) at Lawrence Berkeley National Laboratory. The Advanced Light Source is supported by the Director, Office of Science, Office of Basic Energy Sciences, of the U.S. Department of Energy under Contract No. DE-AC02-05CH11231. We thank Y.-S. Yu and D. Kilcoyne on 5.3.2.2 and D. Vine and T. Tylliszczak on 11.0.2.2 and D. Bothe for their assistance with the STXM experiments.

Notes and references

- 1 H. Yu, Y. J. Kaufman, M. Chin, G. Feingold, L. A. Remer, T. L. Anderson, Y. Balkanski, N. Bellouin, O. Boucher, S. Christopher, P. DeCola, R. Kahn, D. Koch, N. Loeb, M. S. Reddy, M. Schulz, T. Takemura and M. Zhou, *Atmos. Chem. Phys.*, 2006, **6**, 613–666.
- 2 M. B. Baker and T. Peter, *Nature*, 2008, **451**, 299–300.
- 3 P. Forster and V. Ramaswamy, *Changes in atmospheric constituents and in radiative forcing*, Cambridge Univ. Press, New York, 2007.
- 4 T. Storelvmo, C. Hoose and P. Eriksson, *J. Geophys. Res.*, 2011, **116**, D05207.
- 5 D. A. Heggy and M. B. Baker, *Rep. Prog. Phys.*, 2009, **72**, 21.
- 6 K. S. Carslaw, L. A. Lee, C. L. Reddington, K. J. Pringle, A. Rap, P. M. Forster, G. W. Mann, D. V. Spracklen, M. T. Woodhouse, L. A. Regayre and J. R. Pierce, *Nature*, 2013, **503**, 67–71.
- 7 K. Tsigaridis, M. Krol, F. J. Dentener, Y. Balkanski, J. Lathiere, S. Metzger, D. A. Hauglustaine and M. Kanakidou, *Atmos. Chem. Phys.*, 2006, **6**, 5143–5162.
- 8 M. Hallquist, J. C. Wenger, U. Baltensperger, Y. Rudich, D. Simpson, M. Claeys, J. Dommen, N. M. Donahue, C. George, A. H. Goldstein, J. F. Hamilton, H. Herrmann, T. Hoffmann, Y. Iinuma, M. Jang, M. E. Jenkin, J. L. Jimenez, A. Kiendler-Scharr, W. Maenhaut, G. McFiggans, T. F. Mentel, A. Monod, A. S. H. Prevot, J. H. Seinfeld, J. D. Surratt, R. Szmigielski and J. Wildt, *Atmos. Chem. Phys.*, 2009, **9**, 5155–5236.
- 9 J. L. Jimenez, M. R. Canagaratna, N. M. Donahue, A. S. H. Prevot, Q. Zhang, J. H. Kroll, P. F. DeCarlo, J. D. Allan, H. Coe, N. L. Ng, A. C. Aiken, K. S. Docherty, I. M. Ulbrich, A. P. Grieshop, A. L. Robinson, J. Duplissy, J. D. Smith, K. R. Wilson, V. A. Lanz, C. Hueglin, Y. L. Sun, J. Tian, A. Laaksonen, T. Raatikainen, J. Rautiainen, P. Vaattovaara, M. Ehn, M. Kulmala, J. M. Tomlinson, D. R. Collins, M. J. Cubison, E. J. Dunlea, J. A. Huffman, T. B. Onasch, M. R. Alfarra, P. I. Williams, K. Bower, Y. Kondo, J. Schneider, F. Drewnick, S. Borrmann, S. Weimer, K. Demerjian, D. Salcedo, L. Cottrell, R. Griffin, A. Takami, T. Miyoshi, S. Hatakeyama, A. Shimono, J. Y. Sun, Y. M. Zhang, K. Dzepina,

- J. R. Kimmel, D. Sueper, J. T. Jayne, S. C. Herndon, A. M. Trimborn, L. R. Williams, E. C. Wood, A. M. Middlebrook, C. E. Kolb, U. Baltensperger and D. R. Worsnop, *Science*, 2009, **326**, 1525–1529.
- 10 I. G. Kavouras, N. Mihalopoulos and E. G. Stephanou, *Nature*, 1998, **395**, 683–686.
- 11 A. Laaksonen, M. Kulmala, C. D. O'Dowd, J. Joutsensaari, P. Vaattovaara, S. Mikkonen, K. E. J. Lehtinen, L. Sogacheva, M. Dal Maso, P. Aalto, T. Petaja, A. Sogachev, Y. J. Yoon, H. Lihavainen, D. Nilsson, M. C. Facchini, F. Cavalli, S. Fuzzi, T. Hoffmann, F. Arnold, M. Hanke, K. Sellegri, B. Umann, W. Junkermann, H. Coe, J. D. Allan, M. R. Alfarra, D. R. Worsnop, M. L. Riekkola, T. Hyotylainen and Y. Viisanen, *Atmos. Chem. Phys.*, 2008, **8**, 2657–2665.
- 12 H. Kim, B. Barkey and S. E. Paulson, *J. Phys. Chem. A*, 2012, **116**, 6059–6067.
- 13 T. Moise, J. M. Flores and Y. Rudich, *Chem. Rev.*, 2015, **115**, 4400–4439.
- 14 A. Guenther, C. N. Hewitt, D. Erickson, R. Fall, C. Geron, T. Graedel, P. Harley, L. Klinger, M. Lerdau, W. A. McKay, T. Pierce, B. Scholes, R. Steinbrecher, R. Tallamraju, J. Taylor and P. Zimmerman, *J. Geophys. Res.*, 1995, **100**(D5), 8873–8892.
- 15 R. Atkinson and J. Arey, *Atmos. Environ.*, 2003, **37**, S197–S219.
- 16 J. Laothawornkitkul, J. E. Taylor, N. D. Paul and C. N. Hewitt, *New Phytol.*, 2009, **183**, 27–51.
- 17 D. o. E. a. S. A. United Nations, *Population Division (2014), World urbanization prospects: The 2014 revision, highlights*, 2014.
- 18 D. D. Parrish, W. C. Kuster, M. Shao, Y. Yokouchi, Y. Kondo, P. D. Goldan, J. A. de Gouw, M. Koike and T. Shirai, *Atmos. Environ.*, 2009, **43**, 6435–6441.
- 19 T. Berkemeier, M. Shiraiwa, U. Pöschl and T. Koop, *Atmos. Chem. Phys.*, 2014, **14**, 12513–12531.
- 20 T. Koop, J. Bookhold, M. Shiraiwa and U. Pöschl, *Phys. Chem. Chem. Phys.*, 2011, **13**, 19238–19255.
- 21 E. Mikhailov, S. Vlasenko, S. T. Martin, T. Koop and U. Pöschl, *Atmos. Chem. Phys.*, 2009, **9**, 9491–9522.
- 22 P. G. Debenedetti and F. H. Stillinger, *Nature*, 2001, **410**, 259–267.
- 23 B. Zobrist, C. Marcolli, D. A. Pedernera and T. Koop, *Atmos. Chem. Phys.*, 2008, **8**, 5221–5244.
- 24 B. Zobrist, V. Soonsin, B. P. Luo, U. K. Krieger, C. Marcolli, T. Peter and T. Koop, *Phys. Chem. Chem. Phys.*, 2011, **13**, 3514–3526.
- 25 A. Virtanen, J. Joutsensaari, T. Koop, J. Kannosto, P. Yli-Pirila, J. Leskinen, J. M. Makela, J. K. Holopainen, U. Pöschl, M. Kulmala, D. R. Worsnop and A. Laaksonen, *Nature*, 2010, **467**, 824–827.
- 26 E. Saukko, A. T. Lambe, P. Massoli, T. Koop, J. P. Wright, D. R. Croasdale, D. A. Pedernera, T. B. Onasch, A. Laaksonen, P. Davidovits, D. R. Worsnop and A. Virtanen, *Atmos. Chem. Phys.*, 2012, **12**, 7517–7529.
- 27 A. Pajunoja, A. T. Lambe, J. Hakala, N. Rastak, M. J. Cummings, J. F. Brogan, L. Q. Hao, M. Paramonov, J. Hong, N. L. Prisle, J. Malila, S. Romakkaniemi, K. E. J. Lehtinen, A. Laaksonen, M. Kulmala, P. Massoli, T. B. Onasch, N. M. Donahue, I. Riipinen, P. Davidovits, D. R. Worsnop, T. Petaja and A. Virtanen, *Geophys. Res. Lett.*, 2015, **42**, 3063–3068.

- 28 A. P. Bateman, Z. H. Gong, P. F. Liu, B. Sato, G. Cirino, Y. Zhang, P. Artaxo, A. K. Bertram, A. O. Manzi, L. V. Rizzo, R. A. F. Souza, R. A. Zaveri and S. T. Martin, *Nat. Geosci.*, 2016, **9**, 34–37.
- 29 D. M. Lienhard, A. J. Huisman, U. K. Krieger, Y. Rudich, C. Marcolli, B. P. Luo, D. L. Bones, J. P. Reid, A. T. Lambe, M. R. Canagaratna, P. Davidovits, T. B. Onasch, D. R. Worsnop, S. S. Steimer, T. Koop and T. Peter, *Atmos. Chem. Phys.*, 2015, **15**, 13599–13613.
- 30 G. P. Schill, K. Genareau and M. A. Tolbert, *Atmos. Chem. Phys.*, 2015, **15**, 7523–7536.
- 31 B. B. Wang, A. T. Lambe, P. Massoli, T. B. Onasch, P. Davidovits, D. R. Worsnop and D. A. Knopf, *J. Geophys. Res.*, 2012, **117**, D16209.
- 32 T. C. Bond, S. J. Doherty, D. W. Fahey, P. M. Forster, T. Berntsen, B. J. DeAngelo, M. G. Flanner, S. Ghan, B. Karcher, D. Koch, S. Kinne, Y. Kondo, P. K. Quinn, M. C. Sarofim, M. G. Schultz, M. Schulz, C. Venkataraman, H. Zhang, S. Zhang, N. Bellouin, S. K. Guttikunda, P. K. Hopke, M. Z. Jacobson, J. W. Kaiser, Z. Klimont, U. Lohmann, J. P. Schwarz, D. Shindell, T. Storelvmo, S. G. Warren and C. S. Zender, *J. Geophys. Res.*, 2013, **118**, 5380–5552.
- 33 R. K. Chakrabarty, N. D. Beres, H. Moosmüller, S. China, C. Mazzoleni, M. K. Dubey, L. Liu and M. I. Mishchenko, *Sci. Rep.*, 2014, **4**, 5508.
- 34 B. Kärcher, O. Möhler, P. J. DeMott, S. Pechtl and F. Yu, *Atmos. Chem. Phys.*, 2007, **7**, 4203–4227.
- 35 U. Lohmann, *Geophys. Res. Lett.*, 2002, **29**, 1052.
- 36 H. R. Pruppacher and J. D. Klett, *Microphysics of clouds and precipitation*, Springer Netherlands, 1997.
- 37 B. J. Murray, D. O'Sullivan, J. D. Atkinson and M. E. Webb, *Chem. Soc. Rev.*, 2012, **41**, 6519–6554.
- 38 C. Hoose and O. Möhler, *Atmos. Chem. Phys.*, 2012, **12**, 9817–9854.
- 39 D. J. Cziczo, K. D. Froyd, C. Hoose, E. J. Jensen, M. H. Diao, M. A. Zondlo, J. B. Smith, C. H. Twohy and D. M. Murphy, *Science*, 2013, **340**, 1320–1324.
- 40 K. D. Froyd, D. J. Cziczo, C. Hoose, E. J. Jensen, M. H. Diao, M. A. Zondlo, J. B. Smith, C. H. Twohy and D. M. Murphy, in *Nucleation and Atmospheric Aerosols*, ed. P. J. DeMott and C. D. Odowd, Amer. Inst. Physics, Melville, 2013, vol. 1527, pp. 976–978.
- 41 Y. L. Chen, S. M. Kreidenweis, L. M. McInnes, D. C. Rogers and P. J. DeMott, *Geophys. Res. Lett.*, 1998, **25**, 1391–1394.
- 42 D. J. Cziczo, K. D. Froyd, S. J. Gallavardin, O. Moehler, S. Benz, H. Saathoff and D. M. Murphy, *Environ. Res. Lett.*, 2009, **4**, 044013.
- 43 P. J. DeMott, D. J. Cziczo, A. J. Prenni, D. M. Murphy, S. M. Kreidenweis, D. S. Thomson, R. Borys and D. C. Rogers, *Proc. Natl. Acad. Sci. U. S. A.*, 2003, **100**, 14655–14660.
- 44 K. D. Froyd, D. M. Murphy, P. Lawson, D. Baumgardner and R. L. Herman, *Atmos. Chem. Phys.*, 2010, **10**, 209–218.
- 45 K. D. Froyd, D. M. Murphy, T. J. Sanford, D. S. Thomson, J. C. Wilson, L. Pfister and L. Lait, *Atmos. Chem. Phys.*, 2009, **9**, 4363–4385.
- 46 A. J. Prenni, M. D. Petters, S. M. Kreidenweis, C. L. Heald, S. T. Martin, P. Artaxo, R. M. Garland, A. G. Wollny and U. Pöschl, *Nat. Geosci.*, 2009, **2**, 401–404.

- 47 K. A. Pratt, P. J. DeMott, J. R. French, Z. Wang, D. L. Westphal, A. J. Heymsfield, C. H. Twohy, A. J. Prenni and K. A. Prather, *Nat. Geosci.*, 2009, **2**, 397–400.
- 48 K. J. Baustian, D. J. Cziczo, M. E. Wise, K. A. Pratt, G. Kulkarni, A. G. Hallar and M. A. Tolbert, *J. Geophys. Res.*, 2012, **117**, D06217.
- 49 K. J. Baustian, M. E. Wise, E. J. Jensen, G. P. Schill, M. A. Freedman and M. A. Tolbert, *Atmos. Chem. Phys.*, 2013, **13**, 5615–5628.
- 50 K. Ignatius, T. B. Kristensen, E. Jarvinen, L. Nichman, C. Fuchs, H. Gordon, P. Herenz, C. R. Hoyle, J. Duplissy, S. Garimella, A. Dias, C. Frege, N. Hoppel, J. Troestl, R. Wagner, C. Yan, A. Amorim, U. Baltensperger, J. Curtius, N. M. Donahue, M. W. Gallagher, J. Kirkby, M. Kulmala, O. Möhler, H. Saathoff, M. Schnaiter, A. Tome, A. Virtanen, D. Worsnop and F. Stratmann, *Atmos. Chem. Phys.*, 2016, **16**, 6495–6509.
- 51 L. A. Ladino, S. Zhou, J. D. Yakobi-Hancock, D. Aljawhary and J. P. D. Abbatt, *J. Geophys. Res.*, 2014, **119**, 9041–9051.
- 52 O. Möhler, S. Benz, H. Saathoff, M. Schnaiter, R. Wagner, J. Schneider, S. Walter, V. Ebert and S. Wagner, *Environ. Res. Lett.*, 2008, **3**, 025007.
- 53 B. J. Murray, T. W. Wilson, S. Dobbie, Z. Q. Cui, S. Al-Jumur, O. Möhler, M. Schnaiter, R. Wagner, S. Benz, M. Niemand, H. Saathoff, V. Ebert, S. Wagner and B. Kärcher, *Nat. Geosci.*, 2010, **3**, 233–237.
- 54 A. J. Prenni, M. D. Petters, A. Faulhaber, C. M. Carrico, P. J. Ziemann, S. M. Kreidenweis and P. J. DeMott, *Geophys. Res. Lett.*, 2009, **36**, L06808.
- 55 G. P. Schill, D. O. De Haan and M. A. Tolbert, *Environ. Sci. Technol.*, 2014, **48**, 1675–1682.
- 56 R. Wagner, O. Möhler, H. Saathoff, M. Schnaiter, J. Skrotzki, T. Leisner, T. W. Wilson, T. L. Malkin and B. J. Murray, *Atmos. Chem. Phys.*, 2012, **12**, 8589–8610.
- 57 T. W. Wilson, B. J. Murray, R. Wagner, O. Möhler, H. Saathoff, M. Schnaiter, J. Skrotzki, H. C. Price, T. L. Malkin, S. Dobbie and S. Al-Jumur, *Atmos. Chem. Phys.*, 2012, **12**, 8611–8632.
- 58 S. D. Brooks, K. Suter and L. Olivarez, *J. Phys. Chem. A*, 2014, **118**, 10036–10047.
- 59 C. Chou, Z. A. Kanji, O. Stetzer, T. Tritscher, R. Chirico, M. F. Heringa, E. Weingartner, A. S. H. Prévôt, U. Baltensperger and U. Lohmann, *Atmos. Chem. Phys.*, 2013, **13**, 761–772.
- 60 I. Crawford, O. Möhler, M. Schnaiter, H. Saathoff, D. Liu, G. McMeeking, C. Linke, M. Flynn, K. N. Bower, P. J. Connolly, M. W. Gallagher and H. Coe, *Atmos. Chem. Phys.*, 2011, **11**, 9549–9561.
- 61 P. J. DeMott, *J. Appl. Meteorol.*, 1990, **29**, 1072–1079.
- 62 P. J. DeMott, Y. Chen, S. M. Kreidenweis, D. C. Rogers and D. E. Sherman, *Geophys. Res. Lett.*, 1999, **26**, 2429–2432.
- 63 P. J. DeMott, M. D. Petters, A. J. Prenni, C. M. Carrico, S. M. Kreidenweis, J. L. Collett and H. Moosmüller, *J. Geophys. Res.*, 2009, **114**, D16205.
- 64 K. Diehl and S. K. Mitra, *Atmos. Environ.*, 1998, **32**, 3145–3151.
- 65 M. Dymarska, B. J. Murray, L. M. Sun, M. L. Eastwood, D. A. Knopf and A. K. Bertram, *J. Geophys. Res.*, 2006, **111**, D04204.
- 66 A. P. Fornea, S. D. Brooks, J. B. Dooley and A. Saha, *J. Geophys. Res.*, 2009, **114**, D13201.

- 67 B. Friedman, G. Kulkarni, J. Beranek, A. Zelenyuk, J. A. Thornton and D. J. Cziczo, *J. Geophys. Res.*, 2011, **116**, D17203.
- 68 B. Gorbunov, A. Baklanov, N. Kakutkina, H. L. Windsor and R. Toumi, *J. Aerosol Sci.*, 2001, **32**, 199–215.
- 69 Z. A. Kanji and J. P. D. Abbatt, *J. Geophys. Res.*, 2006, **111**, D16204.
- 70 Z. A. Kanji, P. J. DeMott, O. Möhler and J. P. D. Abbatt, *Atmos. Chem. Phys.*, 2011, **11**, 31–41.
- 71 E. D. Kireeva, O. B. Popovicheva, N. M. Persiantseva, T. D. Khokhlova and N. K. Shonija, *Colloid J.*, 2009, **71**, 353–359.
- 72 K. A. Koehler, P. J. DeMott, S. M. Kreidenweis, O. B. Popovicheva, M. D. Petters, C. M. Carrico, E. D. Kireeva, T. D. Khokhlova and N. K. Shonija, *Phys. Chem. Chem. Phys.*, 2009, **11**, 7906–7920.
- 73 G. Kulkarni, S. China, S. Liu, M. Nandasiri, N. Sharma, J. Wilson, A. C. Aiken, D. Chand, A. Laskin, C. Mazzoleni, M. Pekour, J. Shilling, V. Shutthanandan, A. Zelenyuk and R. A. Zaveri, *Geophys. Res. Lett.*, 2016, **43**, 3580–3588.
- 74 O. Möhler, S. Büttner, C. Linke, M. Schnaiter, H. Saathoff, O. Stetzer, R. Wagner, M. Krämer, A. Mangold, V. Ebert and U. Schurath, *J. Geophys. Res.*, 2005, **110**, D11210.
- 75 G. P. Schill, S. H. Jathar, J. K. Kodros, E. J. T. Levin, A. M. Galang, B. Friedman, M. F. Link, D. K. Farmer, J. R. Pierce, S. M. Kreidenweis and P. J. DeMott, *Geophys. Res. Lett.*, 2016, **43**, 5524–5531.
- 76 R. J. Hopkins, A. V. Tivanski, B. D. Marten and M. K. Gilles, *J. Aerosol Sci.*, 2007, **38**, 573–591.
- 77 R. C. Moffet, A. V. Tivanski and M. K. Gilles, in *Fundamentals and Applications in Aerosol Spectroscopy*, ed. R. Signorell and J. P. Reid, Taylor and Francis Books, Inc., Boca Raton, Fla, 2010, pp. 419–462.
- 78 B. B. Wang, A. Laskin, T. Roedel, M. K. Gilles, R. C. Moffet, A. V. Tivanski and D. A. Knopf, *J. Geophys. Res.*, 2012, **117**, D00V19.
- 79 D. A. Knopf, P. A. Alpert, B. Wang, R. E. O'Brien, S. T. Kelly, A. Laskin, M. K. Gilles and R. C. Moffet, *J. Geophys. Res.*, 2014, **119**, 10365–10381.
- 80 M. Shiraiwa, C. Pfrang, T. Koop and U. Pöschl, *Atmos. Chem. Phys.*, 2012, **12**, 2777–2794.
- 81 E. S. Cross, T. B. Onasch, A. Ahern, W. Wrobel, J. G. Slowik, J. Olfert, D. A. Lack, P. Massoli, C. D. Cappa, J. P. Schwarz, J. R. Spackman, D. W. Fahey, A. Sedlacek, A. Trimborn, J. T. Jayne, A. Freedman, L. R. Williams, N. L. Ng, C. Mazzoleni, M. Dubey, B. Brem, G. Kok, R. Subramanian, S. Freitag, A. Clarke, D. Thornhill, L. C. Marr, C. E. Kolb, D. R. Worsnop and P. Davidovits, *Aerosol Sci. Technol.*, 2010, **44**, 592–611.
- 82 J. G. Slowik, E. S. Cross, J.-H. Han, J. Kolucki, P. Davidovits, L. R. Williams, T. B. Onasch, J. T. Jayne, C. E. Kolb and D. R. Worsnop, *Aerosol Sci. Technol.*, 2007, **41**, 734–750.
- 83 A. T. Lambe, A. T. Ahern, J. P. Wright, D. R. Croasdale, P. Davidovits and T. B. Onasch, *J. Aerosol Sci.*, 2015, **79**, 31–39.
- 84 R. Ghazi, H. Tjong, A. Soewono, S. N. Rogak and J. S. Olfert, *Aerosol Sci. Technol.*, 2013, **47**, 395–405.
- 85 C. B. Stipe, B. S. Higgins, D. Lucas, C. P. Koshland and R. F. Sawyer, *Rev. Sci. Instrum.*, 2005, **76**, 023908.
- 86 E. Kang, M. J. Root, D. W. Toohey and W. H. Brune, *Atmos. Chem. Phys.*, 2007, **7**, 5727–5744.

- 87 A. T. Lambe, A. T. Ahern, L. R. Williams, J. G. Slowik, J. P. S. Wong, J. P. D. Abbatt, W. H. Brune, N. L. Ng, J. P. Wright, D. R. Croasdale, D. R. Worsnop, P. Davidovits and T. B. Onasch, *Atmos. Meas. Tech.*, 2011, **4**, 445–461.
- 88 T. B. Onasch, A. Trimborn, E. C. Fortner, J. T. Jayne, G. L. Kok, L. R. Williams, P. Davidovits and D. R. Worsnop, *Aerosol Sci. Technol.*, 2012, **46**, 804–817.
- 89 D. Sueper, *ToF-AMS software downloads*, <http://cires1.colorado.edu/jjimenez-group/ToFAMSResources/ToFSoftware/>.
- 90 M. R. Canagaratna, J. L. Jimenez, J. H. Kroll, Q. Chen, S. H. Kessler, P. Massoli, L. Hildebrandt Ruiz, E. Fortner, L. R. Williams, K. R. Wilson, J. D. Surratt, N. M. Donahue, J. T. Jayne and D. R. Worsnop, *Atmos. Chem. Phys.*, 2015, **15**, 253–272.
- 91 J. Laskin, A. Laskin, P. J. Roach, G. W. Slys, G. A. Anderson, S. A. Nizkorodov, D. L. Bones and L. Q. Nguyen, *Anal. Chem.*, 2010, **82**, 2048–2058.
- 92 V. A. Marple, K. L. Rubow and S. M. Behm, *Aerosol Sci. Technol.*, 1991, **14**, 434–446.
- 93 B. B. Wang and D. A. Knopf, *J. Geophys. Res.*, 2011, **116**, D03205.
- 94 D. A. Knopf, B. Wang, A. Laskin, R. C. Moffet and M. K. Gilles, *Geophys. Res. Lett.*, 2010, **37**, L11803.
- 95 R. C. Moffet, R. E. O'Brien, P. A. Alpert, S. T. Kelly, D. Q. Pham, M. K. Gilles, D. A. Knopf and A. Laskin, *Atmos. Chem. Phys.*, 2016, **16**, 14515–14525.
- 96 R. J. Hopkins, Y. Desyaterik, A. V. Tivanski, R. A. Zaveri, C. M. Berkowitz, T. Tylliszczak, M. K. Gilles and A. Laskin, *J. Geophys. Res.*, 2008, **113**, D04209.
- 97 H. A. Michelsen, A. V. Tivanski, M. K. Gilles, L. H. van Poppel, M. A. Dansson and P. R. Buseck, *Appl. Opt.*, 2007, **46**, 959–977.
- 98 S. Takahama, S. Gilardoni, L. M. Russell and A. L. D. Kilcoyne, *Atmos. Environ.*, 2007, **41**, 9435–9451.
- 99 A. V. Tivanski, R. J. Hopkins, T. Tylliszczak and M. K. Gilles, *J. Phys. Chem. A*, 2007, **111**, 5448–5458.
- 100 A. L. D. Kilcoyne, T. Tylliszczak, W. F. Steele, S. Fakra, P. Hitchcock, K. Franck, E. Anderson, B. Harteneck, E. G. Rightor, G. E. Mitchell, A. P. Hitchcock, L. Yang, T. Warwick and H. Ade, *J. Synchrotron Radiat.*, 2003, **10**, 125–136.
- 101 S. Ghorai, A. Laskin and A. V. Tivanski, *J. Phys. Chem. A*, 2011, **115**, 4373–4380.
- 102 S. Ghorai and A. V. Tivanski, *Anal. Chem.*, 2010, **82**, 9289–9298.
- 103 R. C. Moffet, T. Henn, A. Laskin and M. K. Gilles, *Anal. Chem.*, 2010, **82**, 7906–7914.
- 104 D. M. Murphy and T. Koop, *Q. J. R. Meteorol. Soc.*, 2005, **131**, 1539–1565.
- 105 M. L. Eastwood, S. Cremel, C. Gehrke, E. Girard and A. K. Bertram, *J. Geophys. Res.*, 2008, **113**, D22203.
- 106 M. T. Parsons, J. Mak, S. R. Lipetz and A. K. Bertram, *J. Geophys. Res.*, 2004, **109**, D06212.
- 107 B. Kärcher and J. Ström, *Atmos. Chem. Phys.*, 2003, **3**, 823–838.
- 108 B. Kärcher, J. Hendricks and U. Lohmann, *J. Geophys. Res.*, 2006, **111**, D01205.
- 109 B. Kärcher and U. Lohmann, *J. Geophys. Res.*, 2003, **108**, 4402.
- 110 A. T. Lambe, T. B. Onasch, P. Massoli, D. R. Croasdale, J. P. Wright, A. T. Ahern, L. R. Williams, D. R. Worsnop, W. H. Brune and P. Davidovits, *Atmos. Chem. Phys.*, 2011, **11**, 8913–8928.
- 111 J. H. Kroll, N. M. Donahue, J. L. Jimenez, S. H. Kessler, M. R. Canagaratna, K. R. Wilson, K. E. Altieri, L. R. Mazzoleni, A. S. Wozniak, H. Bluhm,

- E. R. Mysak, J. D. Smith, C. E. Kolb and D. R. Worsnop, *Nat. Chem.*, 2011, **3**, 133–139.
- 112 J. H. Kroll and J. H. Seinfeld, *Atmos. Environ.*, 2008, **42**, 3593–3624.
- 113 A. K. Bertram, S. T. Martin, S. J. Hanna, M. L. Smith, A. Bodsworth, Q. Chen, M. Kuwata, A. Liu, Y. You and S. R. Zorn, *Atmos. Chem. Phys.*, 2011, **11**, 10995–11006.
- 114 D. A. Knopf and Y. J. Rigg, *J. Phys. Chem. A*, 2011, **115**, 762–773.
- 115 T. Koop, B. P. Luo, A. Tsias and T. Peter, *Nature*, 2000, **406**, 611–614.
- 116 T. Koop and B. Zobrist, *Phys. Chem. Chem. Phys.*, 2009, **11**, 10839–10850.
- 117 J. P. D. Abbatt, K. Broekhuizen and P. P. Kumal, *Atmos. Environ.*, 2005, **39**, 4767–4778.
- 118 M. Bilde and B. Svenningsson, *Tellus, Ser. B*, 2004, **56**, 128–134.
- 119 M. D. Petters and S. M. Kreidenweis, *Atmos. Chem. Phys.*, 2007, **7**, 1961–1971.
- 120 J. H. Slade, R. Thalman, J. Wang and D. A. Knopf, *Atmos. Chem. Phys.*, 2015, **15**, 10183–10201.
- 121 B. Wang, D. A. Knopf, S. China, B. W. Arey, T. H. Harder, M. K. Gilles and A. Laskin, *Phys. Chem. Chem. Phys.*, 2016, **18**, 29721–29731.
- 122 K. N. Collier and S. D. Brooks, *J. Phys. Chem. A*, 2016, **120**, 10169–10180.
- 123 J. H. Slade and D. A. Knopf, *Geophys. Res. Lett.*, 2014, **41**, 5297–5306.
- 124 A. M. Arangio, J. H. Slade, T. Berkemeier, U. Pöschl, D. A. Knopf and M. Shiraiwa, *J. Phys. Chem. A*, 2015, **119**, 4533–4544.
- 125 Y. Rudich, N. M. Donahue and T. F. Mentel, *Annu. Rev. Phys. Chem.*, 2007, **58**, 321–352.
- 126 I. J. George and J. P. D. Abbatt, *Nat. Chem.*, 2010, **2**, 713–722.
- 127 Y. You, M. L. Smith, M. J. Song, S. T. Martin and A. K. Bertram, *Int. Rev. Phys. Chem.*, 2014, **33**, 43–77.
- 128 M. Shiraiwa, A. Zuend, A. K. Bertram and J. H. Seinfeld, *Phys. Chem. Chem. Phys.*, 2013, **15**, 11441–11453.
- 129 Q. Chen, Y. J. Liu, N. M. Donahue, J. E. Shilling and S. T. Martin, *Environ. Sci. Technol.*, 2011, **45**, 4763–4770.
- 130 P. F. DeCarlo, J. G. Slowik, D. R. Worsnop, P. Davidovits and J. L. Jimenez, *Aerosol Sci. Technol.*, 2004, **38**, 1185–1205.
- 131 P. Massoli, A. T. Lambe, A. T. Ahern, L. R. Williams, M. Ehn, J. Mikkila, M. R. Canagaratna, W. H. Brune, T. B. Onasch, J. T. Jayne, T. Petaja, M. Kulmala, A. Laaksonen, C. E. Kolb, P. Davidovits and D. R. Worsnop, *Geophys. Res. Lett.*, 2010, **37**, L24801.
- 132 M. Kuwata, S. R. Zorn and S. T. Martin, *Environ. Sci. Technol.*, 2012, **46**, 787–794.
- 133 T. Koop, *Z. Phys. Chem.*, 2004, **218**, 1231–1258.